SPE-175788-MS

Poroperm Characterization and Rock Typing of Tight Carbonate Reservoir Using Core Calibrated Image Perm Technique: Turonian Carbonates in Abu Sennan Field, Western Desert, Egypt, A Case Study

Adly Helba, Wael Ali, and Mohsen Abdel Fattah, Halliburton; Hesham Mokhtar, and Mona Farouk, General Petroleum Company, Egypt

This paper was prepared for presentation at the SPE North Africa Technical Conference and Exhibition held in Cairo, Egypt, 14–16 September 2015.

Abstract

The recent achievement in unconventional reservoirs has established the objective of reevaluating the oil-bearing tight carbonates as potential oil production reservoirs. Of these carbonates, the Turonian Abu Roash D (AR/D) tight limestone in the Abu Sennan field of the Western Desert, Egypt contains oil, but has extremely poor recovery. The challenge in this study is to define the effective parameters that control the various petrophysical attributes of this tight reservoir and their influence on reservoir recovery.

Integrated sedimentological analysis and poroperm characterization was performed based on various data sets, including conventional core analysis, mercury injection tests, and petrographic inspection. A core-calibrated image-perm software algorithm was processed to evaluate the heterogeneity of reservoir pore system and to provide a continuous and azimuthal output of high resolution porosity and permeability.

The AR/D limestone succession (approximately 82 m thick) consists almost entirely of offshore-outer ramp bioclastic wackestone-mudstone facies, with the exception of a reduced reservoir-forming interval (approximately 10 m thick), which consists of inner- to mid-ramp facies. The outer-ramp offshore facies have very poor reservoir quality, with total porosity of less than 9% and permeability values that never exceed 0.1 mD. The reservoir-forming interval begins with storm beds of whole fossil rudstone and bioclastic wackestone, and gradationally terminates upward with inner-ramp shoal beds (5 m thick) of benthic foraminiferal peloidal packstone. The shoal facies measure a noticeably enhanced porosity (15 to 27%) with a relative increase in permeability (up to 2.3 mD). However, a petrographic inspection with resistivity image analysis showed a clear paucity of visible mega- and meso-pores or significant natural open fractures. This means that the reservoir pore system is of the intercrystalline microporosity type, which is confirmed by scanning electron microscope (SEM) and the measured pore throat radii ranging between 1 and 0.005μ. The prevalence of microporosity in the best zone of AR/D reservoir is also evident by a unimodal porosity range distribution shown by an image-perm output. This homogeneous and volumetrically significant microporosity nature may provide a favorable recovery if a suitable fracturing design is applied.

This study highlights the effect of microporosity types on the permeability of tight limestone reservoir, and emphasizes the workflow and benefits of the image-perm technique in evaluating the poroperm system and heterogeneity in the porosity distribution in carbonate reservoirs.

Introduction

The term "unconventional reservoir" covers a wide range of hydrocarbon-bearing formations that generally have a low permeability (less than 0.1 mD) and do not commercially produce without applying stimulation (Passey et al. 2010). Hydrocarbon extraction from these reservoirs is currently increasing as a result of the normal decline of the existing conventional reservoirs. Of this family of reservoirs, the limestone of the Turonian Abu Roash D (AR/D) member was ranked as a secondary target in the proposal of the study vertical well drilled in the southwestern block of the Abu Sennan field, north Western Desert (NWD), Egypt (Fig. 1A).

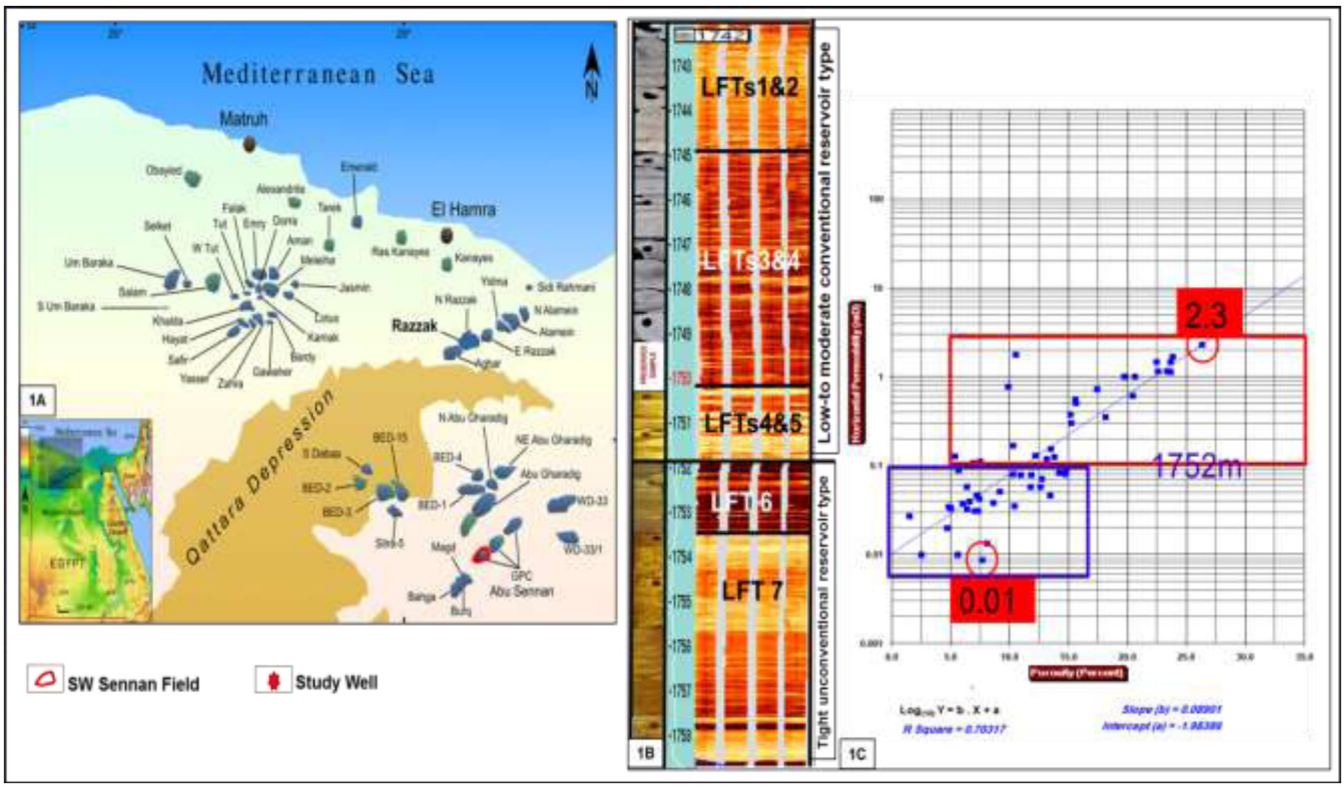

Figure 1—A) Location map of the study well in the southwest block of Abu Sennan field, north Western Desert, Egypt (Zobaa et al., 2011). B) Continuous core (18.16 m length) calibrated with borehole resistivity image covers the reservoir-forming interval of AR/D member. C) Crossplot between porosity percent and horizontal permeability (mD) measured from 56 representative core plugs of the cored interval shown in Fig. 1B.

The penetrated AR/D member, in most intervals, consists of compacted and tight to low permeable limestone that measures an average total porosity of less than 9%, and the permeability value never exceeds 0.1 mD. However, in its lower part, a limestone interval of approximately 10 m thick displays an enhanced porosity of 15 to 27%, with a slight relative increase in permeability to 2.3 mD (Fig. 1B and Fig. 1C). This reservoir-forming interval contains and has produced oil, but with very low recovery.

In the study well, a hydrofracturing job is planned to increase the production of the AR/D limestone reservoir. Consequently, this pre-fracturing reservoir characterization study was performed to distinguish the essential depositional and diagenetic reservoir facies with an emphasis on defining the causative

factors that enhanced or destroyed the reservoir properties. It also tends to identify the reservoir pore system, including its types and nature of distribution and its influence in oil recovery, and define the sweet zones for fracturing.

Database and Workflow

This integrated sedimentological and poroperm analysis was performed based on various data sets gathered from a description of 18.16 m of 4-in. slabbed core covering the AR/D pay zone (Fig. 1B) and supplemented with white light and ultraviolet core photos, conventional core analysis, mercury injection tests, and a petrographic description with SEM inspection of representative core plugs/samples. Core-calibrated resistivity images were analyzed to identify fractures and to extrapolate the recognized core facies in non-cored intervals. An image-perm software algorithm was processed to evaluate the heterogeneity of reservoir pore system and to provide a continuous and azimuthal output of high resolution porosity and permeability. Fig. 2 shows an outline of the workflow used to achieve the objectives of this study.

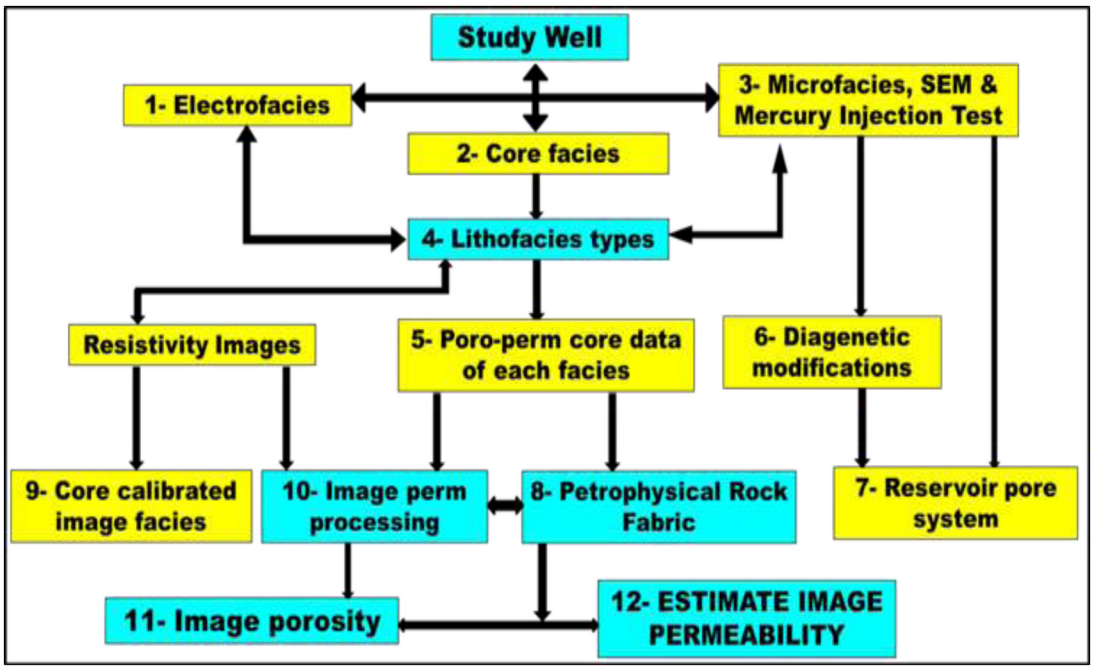

Figure 2—Workflow applied for facies and poroperm characterization of AR/D limestone reservoir.

Geologic and Stratigraphic Setting

The Abu Sennan oil field is among many hydrocarbon-producing fields discovered in the Mesozoic inverted sedimentary basins located in the subsurface of the north Western Desert of Egypt. It is a part of the Abu Gharadig basin; a deep, east-west trending asymmetric graben that initiated as a rift depocenter in Jurassic times, and received a thick pile of Mesozoic sediments in accommodations created through episodic faulting-related subsidence (Bayoumi and Lotfy 1989). During Santonian time, the previous tensional normal faults acquired right-lateral transcurrent motion that produced a system of northeast-southwest compressive ridges, forming inverted basins (Sestini 1995).

The Upper Cretaceous Abu Roash (AR) formation has a wide geographic distribution in north Western Desert basins. It is ranked as one of the rock units with the greatest hydrocarbon potential, and encompasses a number of prolific source- and reservoir-forming members. The formation rests above the

Lower Cenomanian Bahariya formation, and below the Upper Senonian Khoman Chalk (Fig. 3A). It is primarily represented by a sequence of alternating limestone and shale units with sandstone interbeds, and consists of seven informal members assigned, from top to base as AR/A to AR/G (Fig. 3A). The AR/A, AR/C, AR/E, and AR/G members are largely clastics, whereas the AR/B, AR/D, and AR/F members are carbonate dominating (Norton 1967).

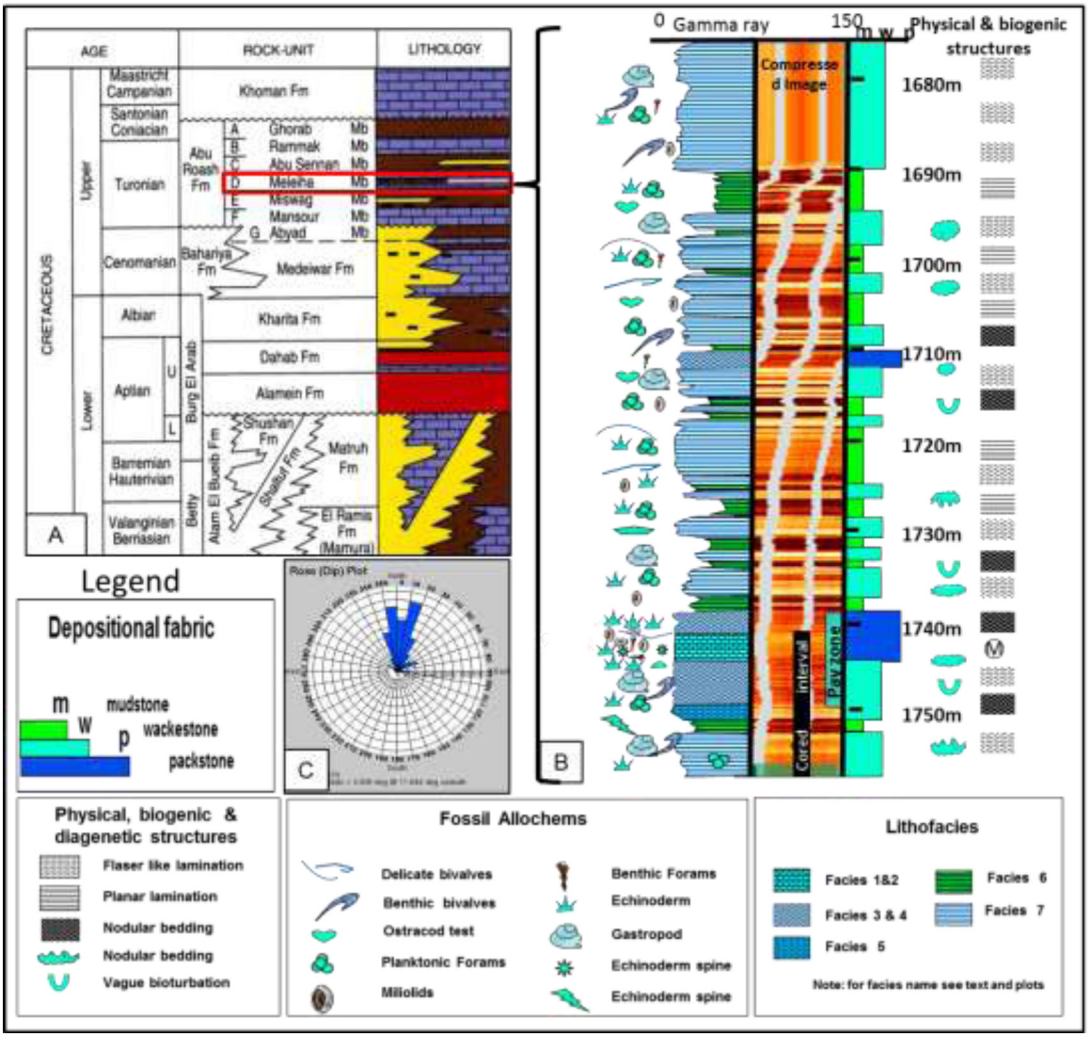

Figure 3—A) General rock stratigraphic classification and nomenclatures of the Cretaceous sedimentary succession applied in north Western Desert, Egypt. B) Facies types, fossil assemblage, depositional fabric, and primary structures characterizing the penetrated limestone-shale succession of AR/D member in the study well. C) Rose diagram displays northward dip azimuths of the picked AR/D limestone beds with average dip attitude measuring 3°/N12°E.

In the southwestern block of Abu Sennan field, the study well encountered the target Turonian AR/D limestone in the measured depth interval of 1676.9 to 1758.8 m, with a total penetrated thickness of approximately 81.9 m; the oil-bearing pay zone exists in the lower part, and begins at the measured depth of 1740 to 1750 m (Fig. 3B). The member consists of thick to very thick bodies of fossiliferous limestone that are separated from one another by thin, and occasionally very thick (up to 5 m), intervals of calcareous mudstone and shale (Fig. 3B). The limestone bodies commonly consist of nodular and lenticular beds that are internally massive to bioturbated, and mostly compacted with numerous sinuous pressure solution seams that are frequently draped by dark brown argillaceous matter with scattered pyrite and dolomite, and stained by organic matter or residual hydrocarbons. The limestone rock is gray to light gray, almost

hard, in parts argillaceous or dolomitic and occasionally siliceous. It is invariably fossiliferous with echinoids, large benthic forams, and few algal fragments, especially in the pay- forming interval. Whole shells of pelecypods and gastropods are well preserved in the lower part of the pay zone, whereas scattered planktonic forams and echinoid fragments are observed in the fine-grained non-pay forming intervals. The essential limestone and shale beds are nearly horizontal or dipping gently in directions swinging from north-northeast to north-northwest, with a computed average dip attitude measuring 3°/N12° E (Fig. 3C).

AR/D Lithofacies Types

The integrated facies analysis from core slabs, thin sections, and core-calibrated image/open hole logs identified seven main lithofacies types (LFT) building the AR/D member (Fig. 3B). They are primarily of the limestone family; the majority belong to the wackestone and lime-mudstone classes, except limited intervals that consist of grain-supported packstone/rudstone. The individual lithofacies types, key attributes, and mode of formation are described and interpreted in the following subsections.

LFT-1: Massive-Bedded Foraminiferal Peloidal Packstone

Description. This LFT has a very limited vertical distribution in AR/D succession (Fig. 3B). It is recorded only in the measured depth interval from 1742.40 to 1744.48 m (approximately 2.08 m thick); it forms the topmost and relatively best zone of the AR/D reservoir interval in terms of poroperm property, recorded resistivity, and resistivity separation (Fig. 4A, red rectangle). The facies rock ranges from light gray to gray; it is hard, medium- to thick-bedded, internally massive with irregular flaser-like bed boundaries, and few sinuous dark pressure solution seams (Fig. 4B). In thin sections, the rock is grain-supported packstone, medium- to coarse-grained, and moderately- to well-sorted (Fig. 5A). It consists of fossil particles and behamite peloids set in micrite matrix with microspars and, in parts, orthospar cement (Fig. 5A-C). Fossils are abundant and diversified and include large- and small-tests of miliolids, peneroplids, and textularids with other benthic forams, echinoid plates, and algal fragments with scattered molluscan particles and molds (Fig. 5A-C). The majority of foram tests and algal particles are partially or completely micritized; their chambers are almost occupied with microspar and/or orthospar (Fig. 5B). The echinoderm fragments are either partially micritized and/or partially recrystallized, accompanied with syntaxial calcite overgrowth (Fig. 5A). Calcitic molds with a distinct micrite rind are also encountered and partially derived from dissolved aragonitic shells. Except for a very few, small, and isolated intraparticles solution vugs, as well as few irregular microscopic open fractures, almost all inter-and intra-particles pore spaces are completely occluded with micrite, microspar, and, in discrete parts, orthospar.

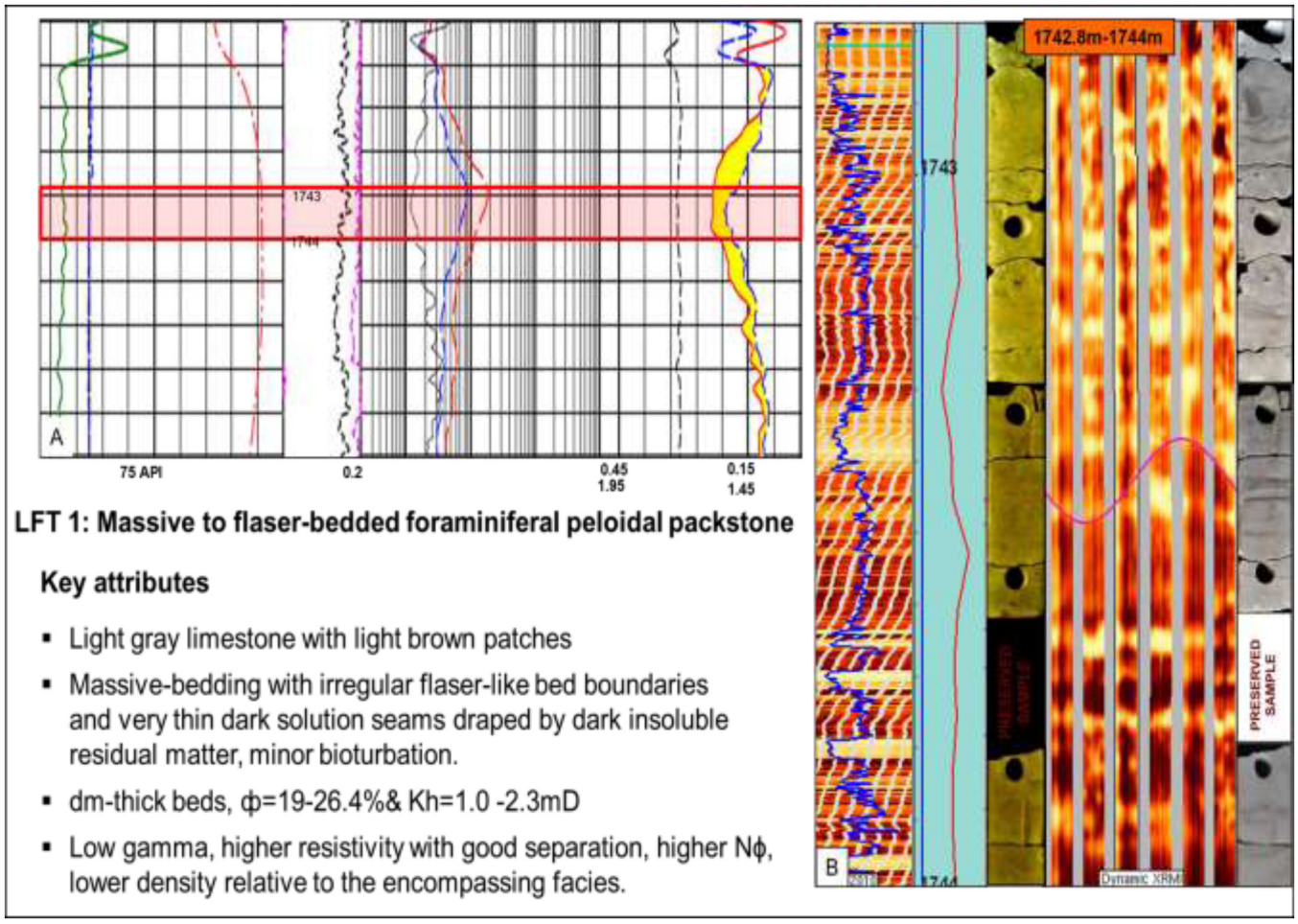

Figure 4—Openhole logs responses (A) and core-calibrated dynamic image (B), displaying the key attributes of the recognized LFT-1.

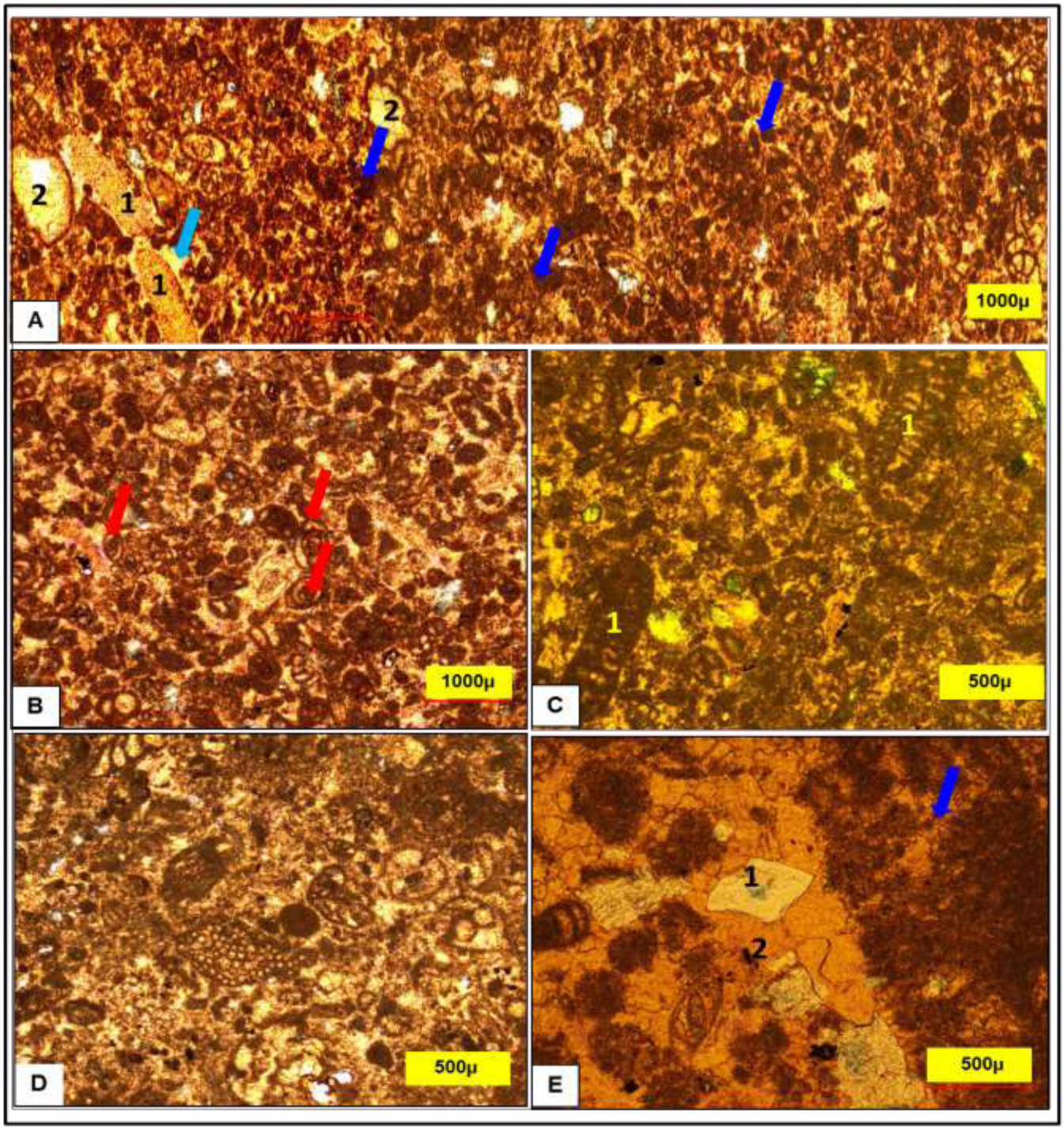

Figure 5—A) Microscopic panorama of LFT-1; foraminiferal peloidal packstone consisting essentially of large benthic forams, echinoderm particles (1) and behamite peloids (blue arrows) with calcitic molds (2) set in micrite matrix with microspar. Most echinoid particles are recrystallized with syntaxial calcite overgrowth (cyan arrow), PPL. B) Close up view of LFT-1 shows grain- supported fabric, good sorting, and abundant micritic walled quinqueloculins (red arrows), triloculins, and other benthic tests with rotten bioclasts set in micro- and pseudo-spar, PPL. C) Different sections of Peneroplis tests (1) mixed with behamite peloids, PPL. D) Relative increase in selective recrystallization in LFT-2 possessing grain-supporting fabric, good sorting, and abundance of micritic walled miliolids and algal particles set in micro- and pseudo-spar, PPL. E) Relative increase in blocky spar cementation (2) with growth of late-stage baroque dolomite (1) in LFT-2 compared with LFT-1, PPL (PPL= plane polarized light).

Interpretation. The medium- to coarse-sandy grain size, well-sorting, and grain-supporting fabric of this facies reflect its bed-load accumulation under a relatively high energy condition and above the fair

weather wave base (FWWB). The abundance and diversity of fauna and presence of echinoderms and algae indicate open water circulation and photic environment, whereas the abundance of large miliolids and textularids suggests shallow water palaeobathymetry (5 to 15 m) (Arnaud-Vanneau 1980, Kovacs 2005). These depositional processes and physical/ecological conditions prevail in shoal, beach, and shallow shelf lagoon (Wilson 1972).

LFT-2: Recrystallized Bioclastic Peloidal Packstone

Description. The LFT-2 has also a narrow vertical distribution in the AR/D succession (Fig. 3B). It is logged only in the pay section with a cumulative thickness of approximately 4.73 m. It rests above and below the rock of LFT-1, and intercalates with thin intervals of LFT-3 and LFT-4. It possesses nearly the same bedding nature, depositional fabric/texture, and allochem types/faunal content of LFT-1 (Fig. 6B), but with a relative increase in echinoids and molluscan particles, pressure solution seams, and more growth of selective calcite recrystallization and cementation with scattered baroque dolomite (Fig. 5D and E). These diagenetic alterations caused a relative reduction in total porosity (ϕ approximately 10 to 18%) and permeability (Kh approximately 0.1 to 1 mD), as compared with LFT-1 (Fig. 6A, red rectangles).

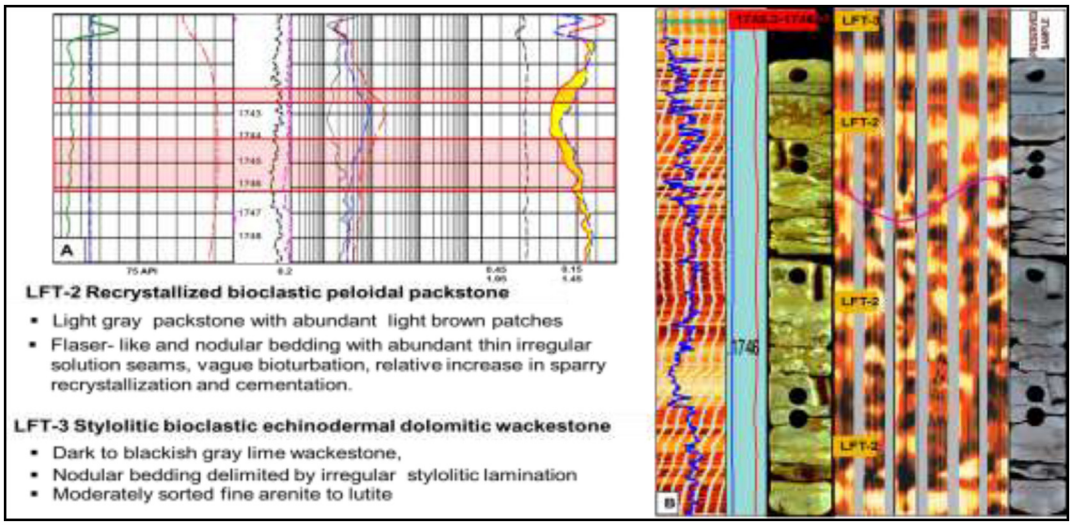

Figure 6—Openhole logs responses (A) and core-calibrated dynamic image (B) displaying the key attributes of the recognized LFT-2 and LFT-3.

Interpretation. Like LFT-1, this rock type was formed through bed-load sedimentation under a relatively moderate to high energy condition and above the FWWB in a shallow open and photic coastal marine environment as inner-ramp shoal.

LFT-3: Stylolitic Echinodermal Dolomitic Wackestone-Mudstone

Description. This rock type occurs only in the pay interval where it forms thin to medium-thick irregular beds and lenses (5 to 20 cm thick), intercalating with LFT-2 and LFT-4 (Fig. 3B). Its rock is dark brown to blackish gray, weak, with frequent irregular stylolites (Fig. 6B). It is matrix-supported and moderately-sorted dolomitic wackestone consisting of fragmented echinoid plates and molluscan casts, with delicate pelecypod shells and few micritic walled forams (Fig. 7A-C). These skeletal particles concentrate and feebly align in discontinuous pockets or sub-parallel bands separated by fossil- poor micrite-laminae, and are set in micrite matrix with microspars and, in parts, orthospar with abundant sucrose- and few baroque-dolomite rhombs (Fig. 7B and C).

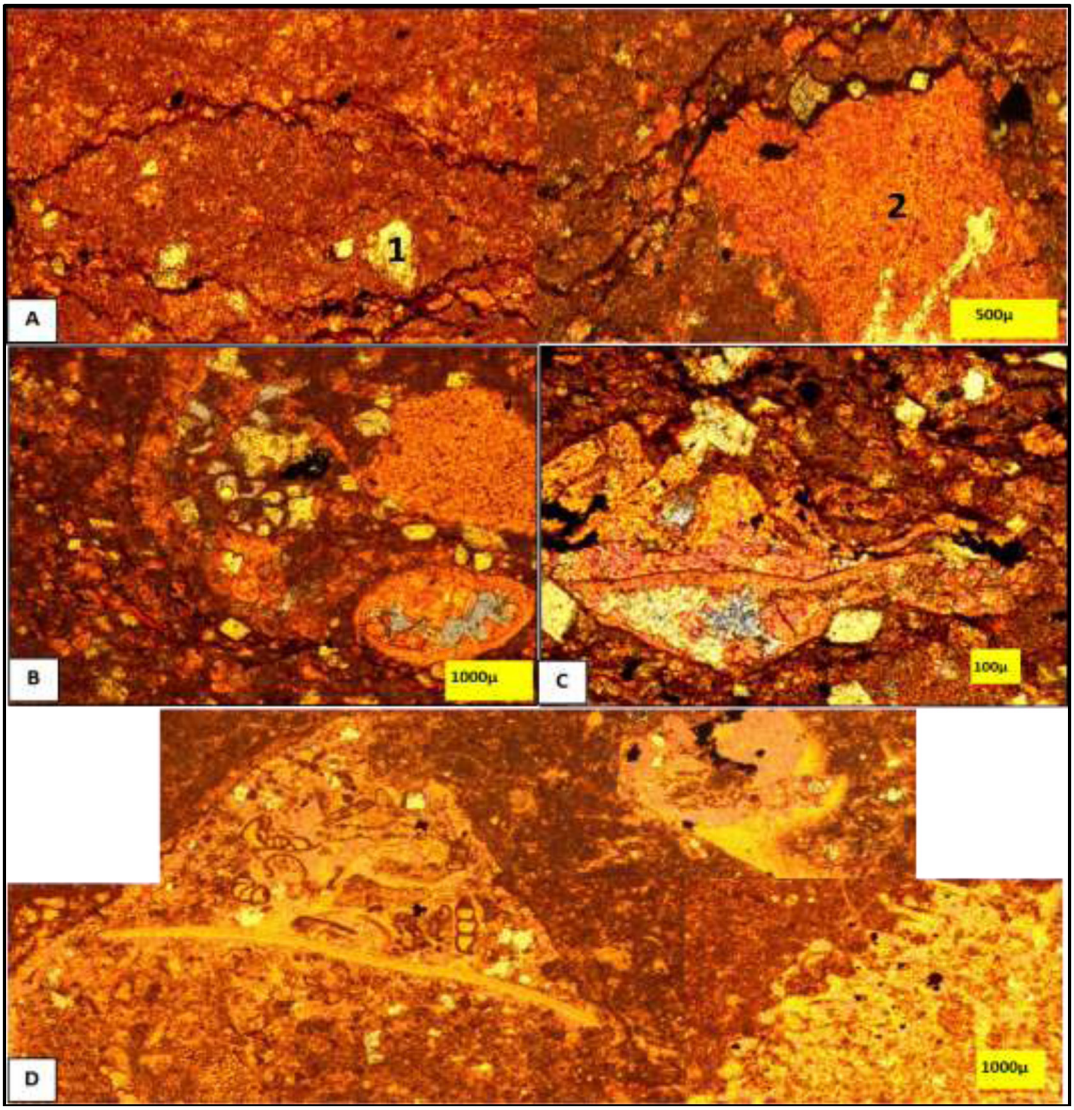

Figure 7—A) Microscopic panorama shows mud-supporting fabric, fragmented echinoid plates (2), and frequent pressure solution seams with saddle dolomites (1) characterizing LFT-3, PPL. B) Feebly aligned delicate bivalves and echinoid fragments floating in micrite matrix with microspar and abundant dolomite, PPL. C) Populations of molluscan shells, delicate bivalves and echinoid plates in small pockets surrounded by fossil poor lime-mud, solution seams, and baroque dolomite characterize LFT-3, PPL. D) Microscopic panorama shows mud-supported floatstone fabric, poor sorting with polymodal sizes (siltite, arenite and rudite), and types of fossil allochems characterizing of LFT-4 (skeletal wackestone to floatstone), PPL.

Interpretation. The silty- to very coarse-sandy grain size, moderate to poor sorting, and mud-supporting fabric of this facies reflect its accumulation from both bed- and suspension-loads under fluctuating energy conditions below the FWWB. The abundance of echinoids and delicate bivalves and paucity of miliolids and textularids indicate open water circulation and photic environment (Arnaud-Vanneau 1980, Kovács 2005). The fragmentation and concentration with weak alignment of fossils in pockets and sub-parallel laminae may reflect accumulation through intermittent short-lived storms, followed by a deposition from suspension under decelerating energy condition. This mode of deposition and environmental conditions are common across mid-ramp and distal inner-ramp belts (Aigner 1985).

LFT-4: Flaser- and Nodular-Bedded Skeletal Floatstone

Description. This facies type forms a thick (approximately 2.8 m) interval in the lower part of the AR/D pay zone, and another interval (approximately 0.91 m thick) near the top of the zone (Fig. 3B). Above the

pay zone, it is also identified in another interval (approximately 1.92 m thick) in the middle part of AR/D member (Fig. 3B). The rock is light gray to gray, hard, medium- to thick-bedded, with irregular flaser-like bed boundaries draped by thin dark-gray marl and winding dark pressure solution seams. It is internally massive and nodular with vague bioturbation traces (Fig. 8). The facies is wackestone to floatstone and poorly sorted, with very fine to medium sandy-sized fossil allochems forming with micrite a groundmass hosting scattered large-sized particles of mollusks, echinoids, and algae (Fig. 7D). The matrix-forming fossils consist primarily of small benthic forams, ostracod valves, other skeletal siltites, and behamite peloids set in a micrite matrix with microspars and few large crystals of saddle dolomite (Fig. 7D). This facies types is poorer in reservoir poroperm property, as compared with LFT-1 and LFT-2 (Fig. 8A, blue rectangle). Its measured total porosity is invariably less than 15%, with horizontal permeability values ranging between 0.1 and 0.01 mD.

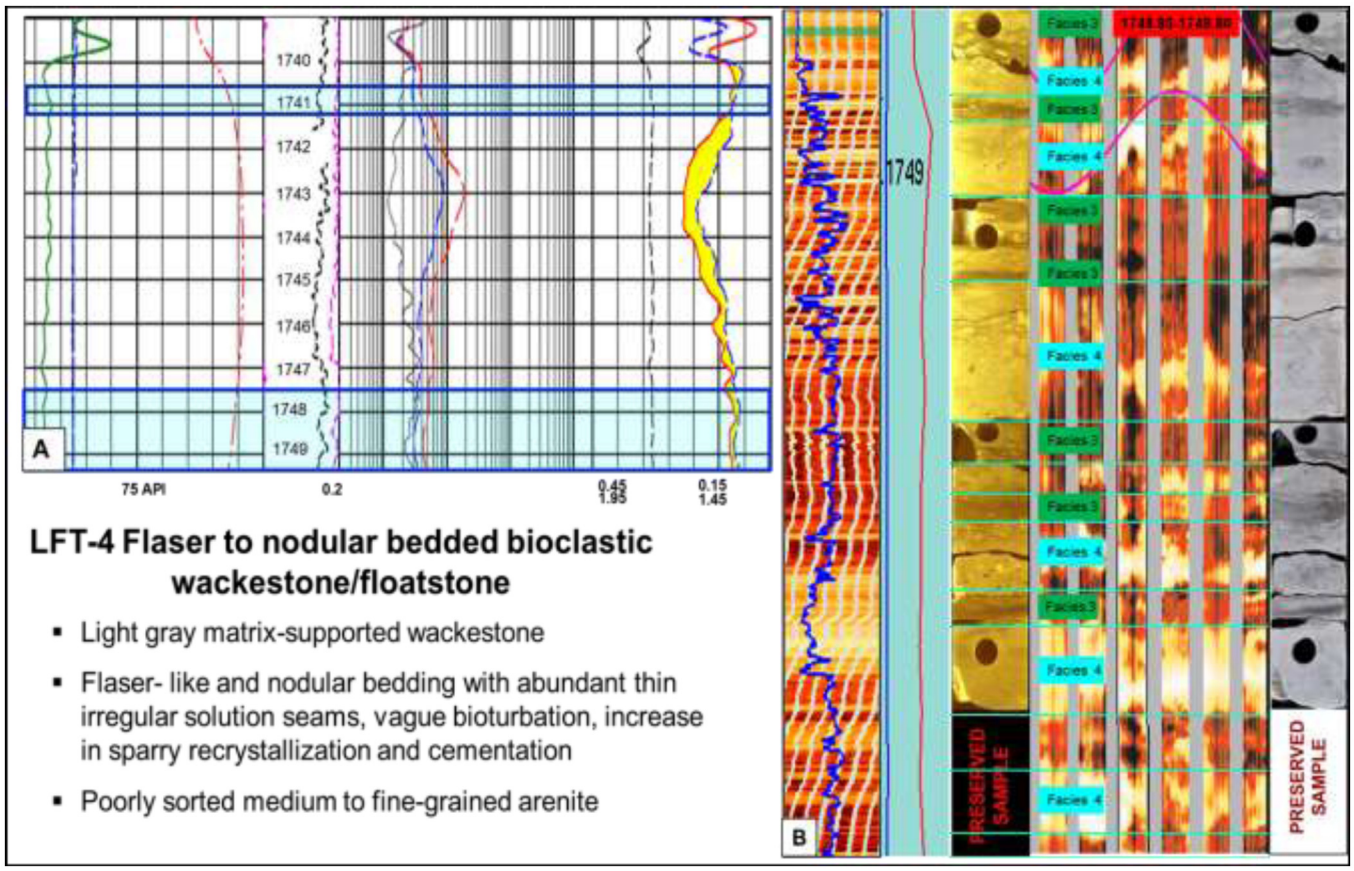

Figure 8—Openhole logs responses (A) and core-calibrated dynamic image (B), displaying the key attributes of the recognized LFT-4.

Interpretation. The mud-rich floatstone fabric and poor sorting with bimodal particles size characterizing this facies indicate its formation through a temporary fluctuating energy condition as momentary storms and below the FWWB. Large-sized shells, especially mollusks, commonly live in high energy environments, and the small-sized benthic forams and ostracods normally inhabit low energy muddy environment. Consequently, its combination in one rock type reflects the delivery of those quiet energy small fossils into energetic setting and mixing them with large shells by short-lived storms, and then rapidly deposited under breaking energy conditions as tempestites (Aigner 1985, Palermo et al. 2010). The nodular bedding style of this facies is attributable to bioturbation with diagenetic overprinting, represented by stylolitic seams around the contacts between limestone nodules and marl drapes. This nodular/flaser bedding is a common style for mid- to outer-ramp limestone deposits.

LFT-5: Lenticular-Bedded Whole Fossil Rudstone

Description. The LFT-5 forms the basal part of the pay zone with a penetrated thickness of approximately 1.65 m (Fig. 3B). The rock is brownish to light gray, hard, very coarse sandy to rudite in size, and yields mega-fossils. It is medium- to thick-bedded with irregular bed boundaries, internally massive and nodular, and commonly dissected by erratic fine calcite veins (Fig. 9B). Microscopically, it is very poorly sorted muddy rudstone consisting of un-abraded and ruditic-sized pelecypods, gastropods, and echinoids rooted in a groundmass of micrite matrix, microspars and silty-sized bio-detritus, small benthic forams, and ostracods (Fig. 10A). The thick aragonitic molluscan shells are invariably dissolved with its moldic cavities filled by several generations of non-feroan and feroan orthospars being partially replaced by baroque dolomite and/or spherulitic quartz (Fig. 10A). This pervasive recrystallization and cementation by various authigenic minerals explains the reduction in poroperm property of this rock type relative to LFT-1 and LFT-2 (Fig. 9A, red rectangle).

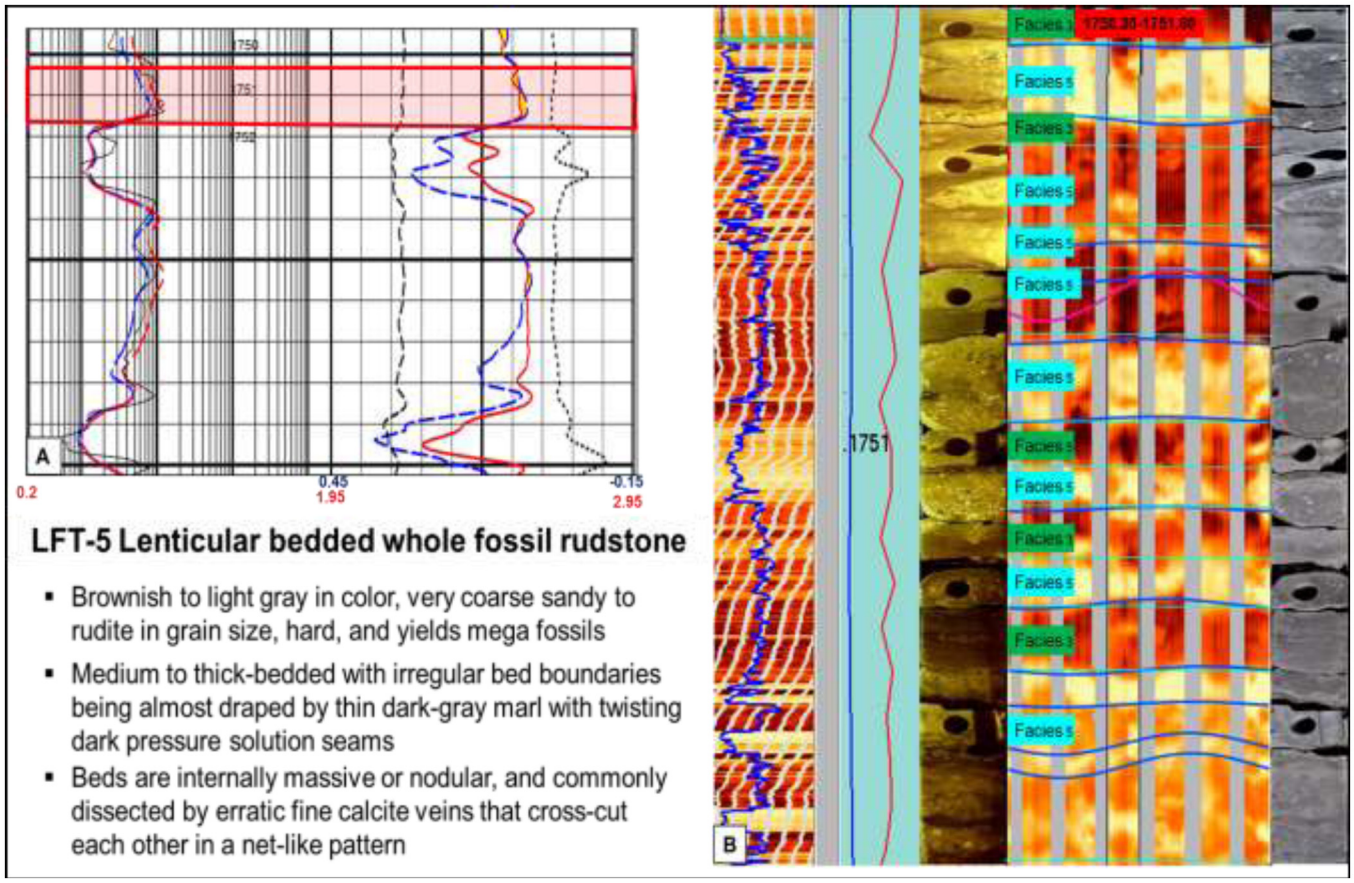

Figure 9—Openhole logs responses (A) and core-calibrated dynamic image (B), displaying the key attributes of the recognized LFT-5.

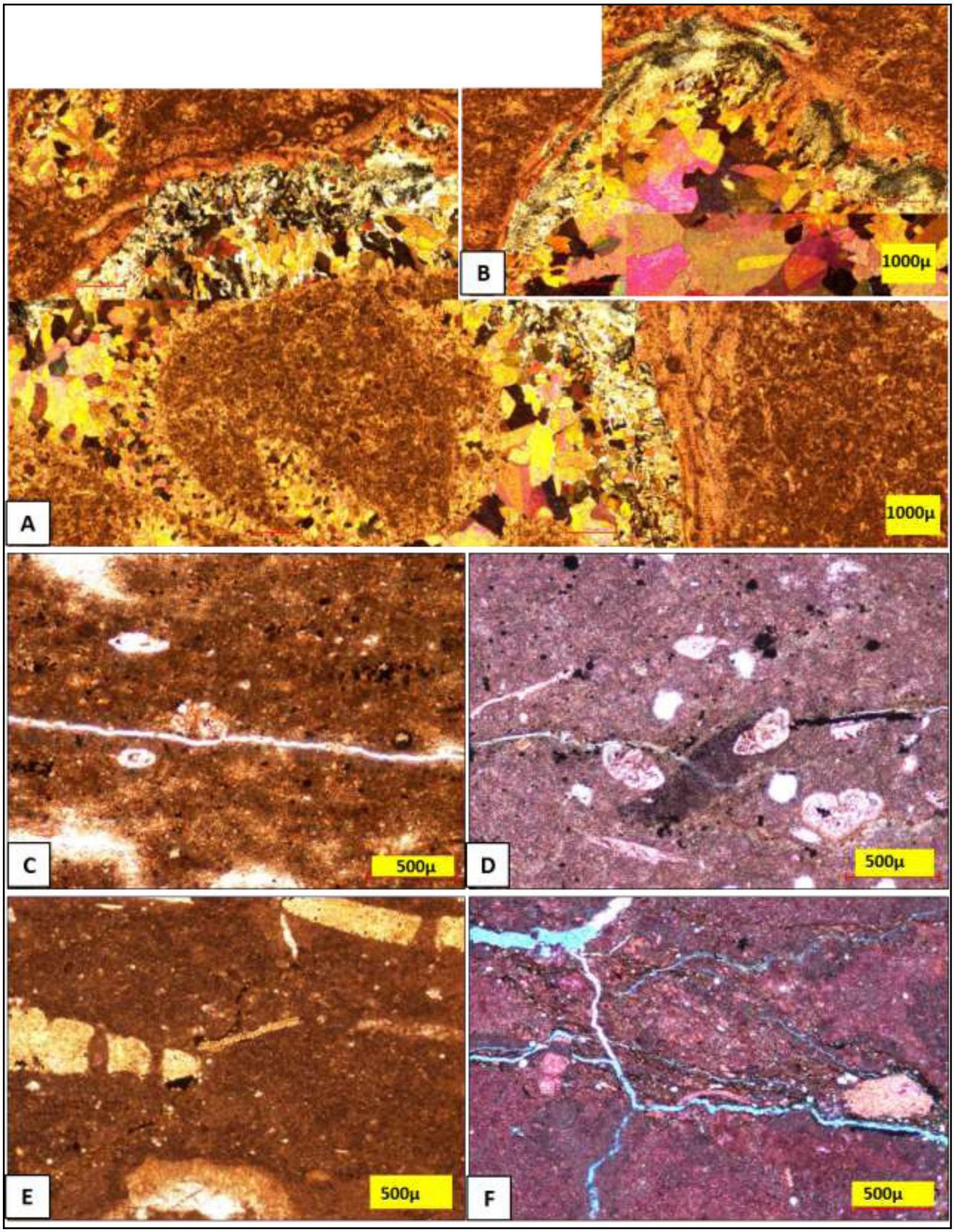

Figure 10—A) and B) Microscopic panoramas show the poor sorting and bimodal size (siltite, rudite) characterizing LFT-5, consisting mainly of thick-shelled, gastropod (A) and pelecypod (B), CN. The original aragonitic shells are dissolved, and its moldic cavities are filled by drusy mosaic orthospars and spherulitic quartz. C) LFT-6 consists of argillaceous micrite matrix with microspar hosting scattered ostracods, undefined fossil molds, some planktonic forams, and clots of framboidal pyrite with microscopic calcite veins. D) and E) LFT-7 Sandy bioclastic wackestone-mudstone consisting of planktonic forams (D), delicate bivalves (D), echinoids fragments (E), with silty-sized quartz grains, PPL. (D) set in micrite matrix. F) Desiccation of LFT-7 by a network of irregular open microfractures postdating dark pressure solution seams, PPL (CN=crossed nicols).

Interpretation. As with LFT-4, the primary criteria of this facies includes muddy rudstone fabric, and poor sorting with bimodal size and abundance of whole fossils of mollusks and echinoderms indicate its formation above the storm wave base (SWB), under intermittent high energy conditions as momentary storms in a mid-ramp environment.

LFT-6: Planar- and Lenticular-Bedded Argillaceous Bioclastic Lime Mudstone

Description. The LFT-6 has a wide vertical distribution in the AR/D succession. It forms several thin to thick intervals (commonly 20 to 150 cm thick) that invariably alternate with intervals of LFT-7. It is not recorded in the pay zone, and its thickest occurrence (up to 4.5 m thick) is identified in the upper part of AR/D member (Fig. 3B). The rock is brownish- to blackish-gray, weak, very fine-grained, internally massive or with faint lamination and isolated small calcareous nodules, and is commonly dissected and locally brecciated by irregular intersecting narrow calcite veins (Fig. 11A and B). The rock is argillaceous lime mudstone consisting of argillaceous micrite matrix hosting scattered echinoid spines and plates, and some planktonic forams with clusters of framboidal pyrite (Fig. 10C).

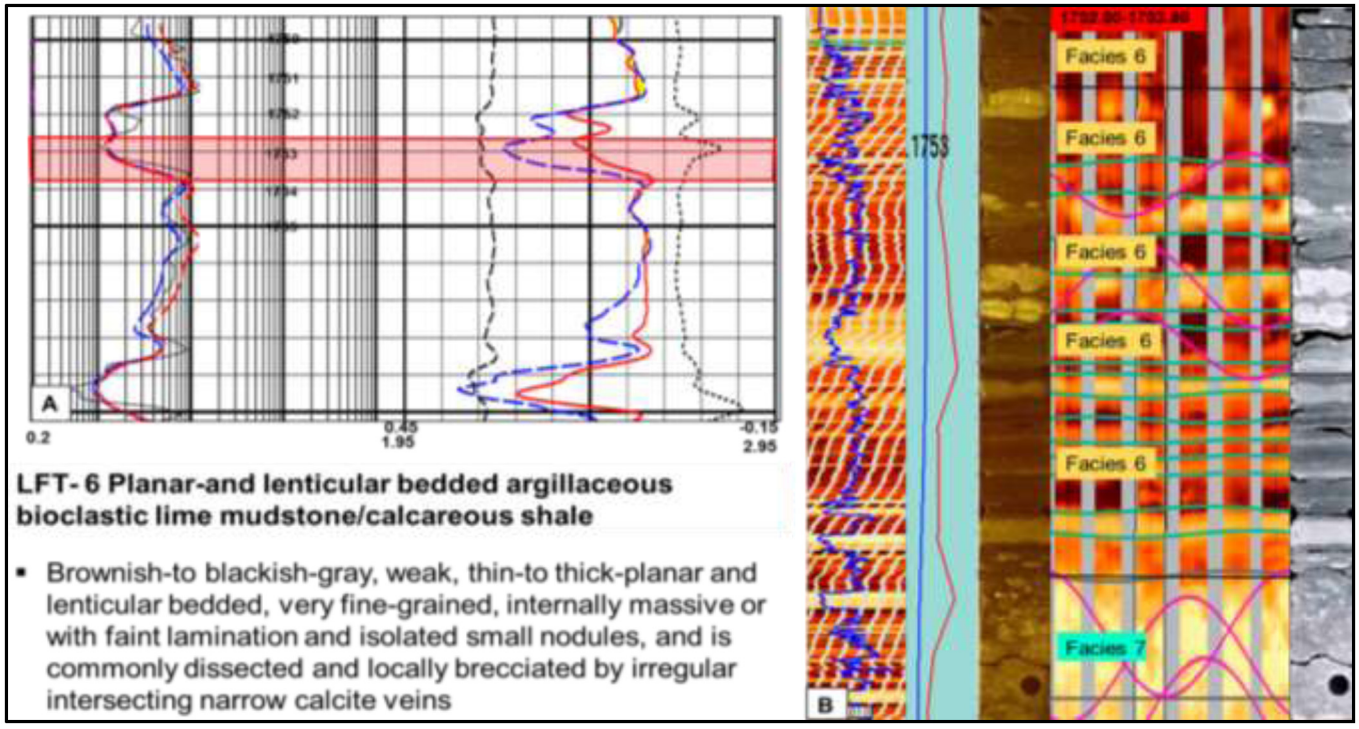

Figure 11—Openhole logs responses (A) and core-calibrated dynamic image (B), displaying the key attributes of the recognized LFT-6.

Interpretation. The overall very fine-grain size and the mud supporting fabric with fine-parallel lamination indicate a deposition from suspension in a calm water environment below the SWB. The presence of echinoids and planktonic forams reflects open marine water circulation. These depositional conditions and processes commonly prevail in open marine offshore and outer ramp environments.

LFT-7: Flaser- and Nodular-Bedded Bioclastic Echinodermal Wackestone-Mudstone

Description. The LFT-7 is the most common rock type in the AR/D succession. It forms medium to very thick bodies that alternate with intervals of LFT-6, building the remainder of the AR/D succession above and below the pay zone (Fig. 3B). The facies rock is light gray to gray, thin- to thick-bedded, very fine-grained, and rigorously compacted. The beds are either internally massive with vague bioturbation or faintly laminated (Fig. 12A and B). It is lime mudstone to wackestone, consisting of micrite matrix and hosting few echinoid plates and spines, planktonic forams, ostracods, and molluscan shells and molds

(Fig. 10D and E). In some intervals, the matrix is slightly argillaceous, and locally contains scattered silty to fine-sandy sized quartz and glauconite grains (Fig. 10D). The rock is very tight with no visible inter- and intra-particles pores, except in a few beds; it is dissected and crackled by irregular and intersecting open microscopic fractures (Fig. 10F).

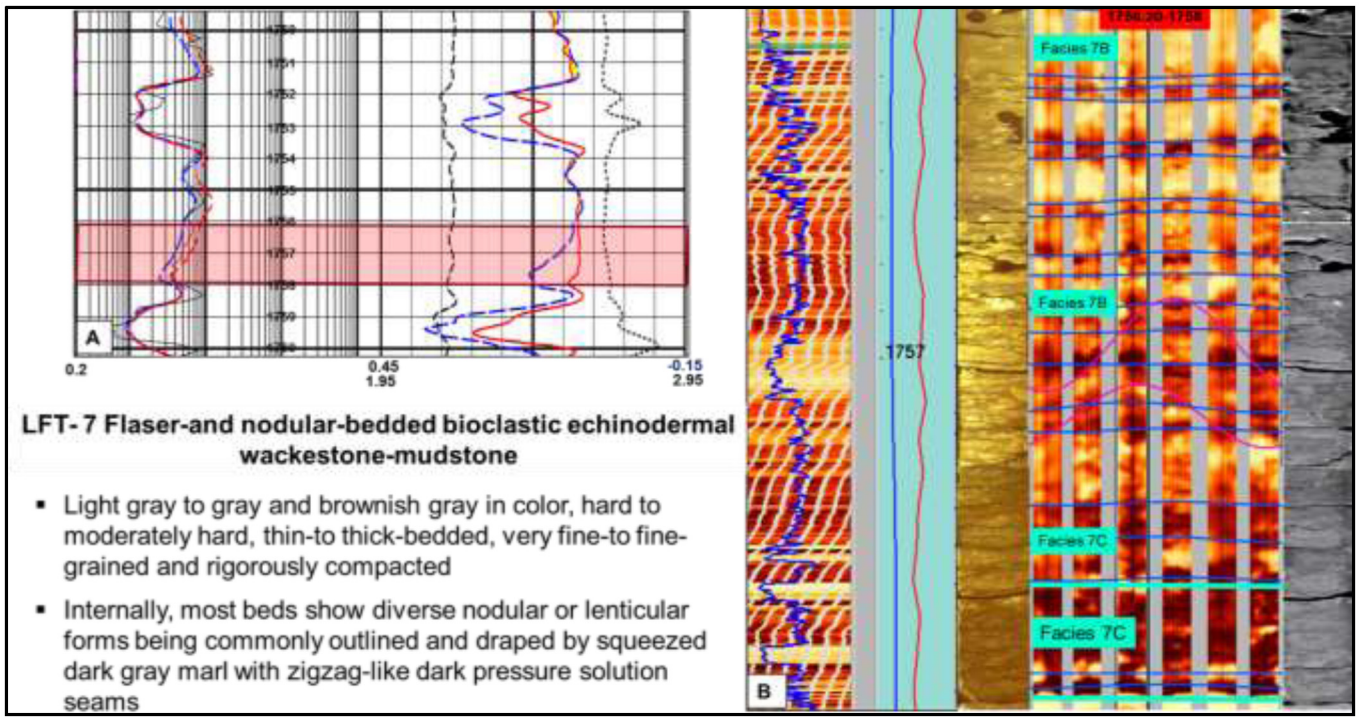

Figure 12—Openhole logs responses (A) and core-calibrated dynamic image (B), displaying the key attributes of the recognized LFT-7.

Interpretation. As with LFT-6, the dominance of lime mud, lutitic-sized components, and matrix-supporting fabric, occasionally with fine-lamination and vague bioturbation, reflects low-energy suspension sedimentation below the SWB background. The presence of echinoids, delicate bivalves, and planktonic forams indicates an open marine condition. However, the local presence of scattered silty-sized quartz and glauconite grains with local concentration of fossils in pockets may reflect intermittent disturbance, reworking, and delivering exotic quartz grains by short-lived storm action.

AR/D Facies Associations and Depositional Model

The recognized AR/D lithofacies types with its assemblages of fauna, sedimentary structures, and depositional fabrics/textures are all regularly reported among the distinctive facies belts of the carbonate ramp model (Ahr 1973, Read 1985, Wright and Burchette 1998). The near-absence of reef-building organisms and the vertical gradational transition from high energy/storm facies (LFT-1 through LFT-5) to low-energy offshore facies (LFT-6 and LFT-7) without a concrete signature for a drastic bathymetric change substantiate a ramp depositional setting for AR/D carbonates. Relying on the genetic relation between AR/D facies types and its vertical stacking pattern, the AR/D facies sequence is differentiated into three facies associations (FA), representing different adjacent sub-environments across the ramp basin (Fig. 13).

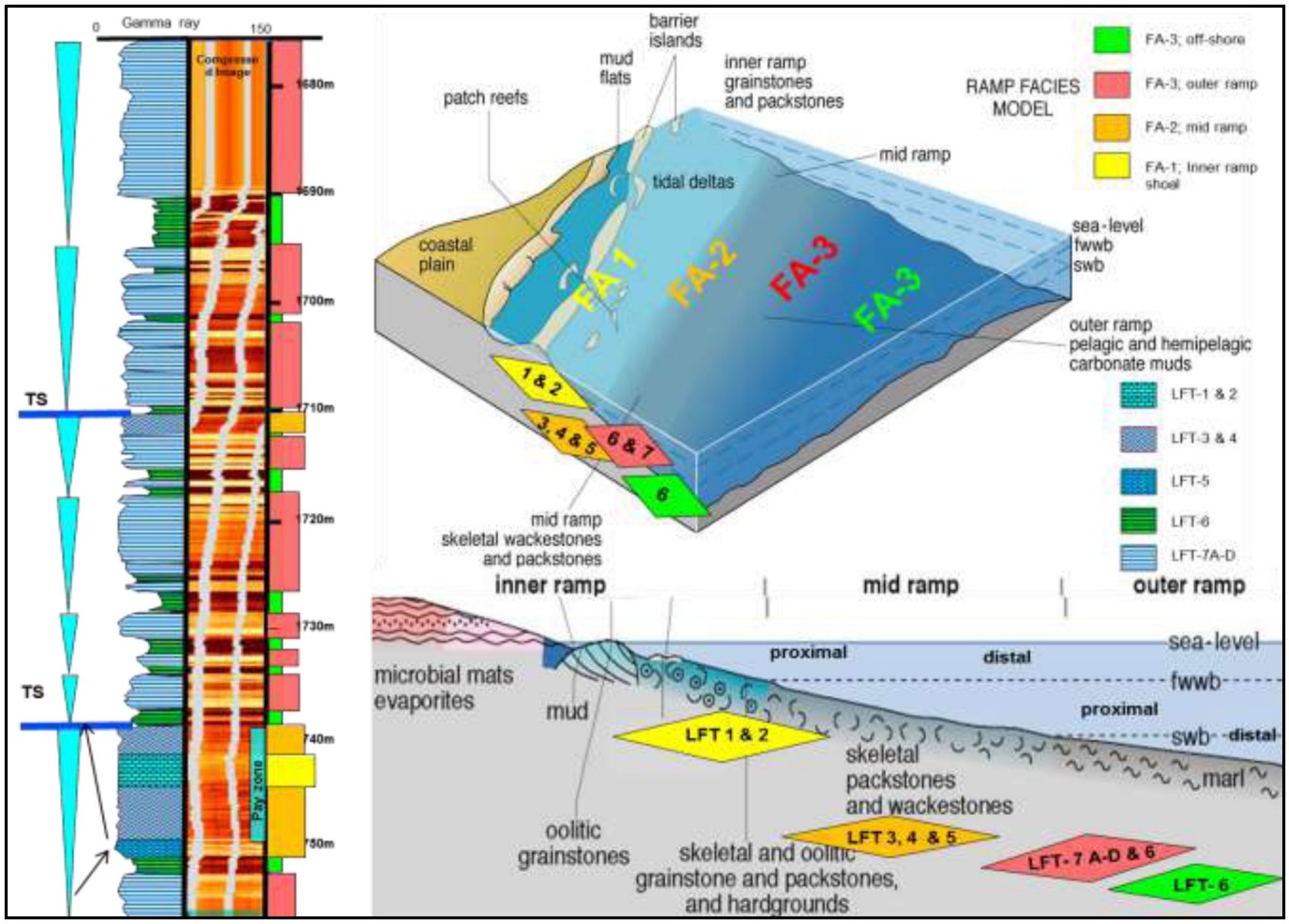

Figure 13—Depositional model for AR/D carbonates that mostly accumulated in outer-ramp offshore belt, except its lower pay-forming part being deposited in shoal and mid-ramp belts.

FA-1: Inner Ramp Shoal Association. This association shared with the least portion in the accretion of the AR/D carbonate succession (Fig. 13). It built only an approximately 7 m thick section in the lower part of the member. However, this small section forms relatively the best zone of the AR/D pay interval in terms of reservoir quality. The association is formed of LFT-1 and LFT-2, which have distinctive good sorting, grain-supporting, and diversified faunal assemblage mixed with abundant peloids, which reflect its accumulation in shallow, open, and agitated marine water environment. It terminates a prograding shoaling-upward regressive segment of a transgressive-regressive ramp cycle (Fig. 13). It rests gradationally above a mid-ramp facies association (FA-2) that, in turn, grades downward to offshore-outer ramp facies assemblages (FA-3).

FA-2: Mid Ramp Association. The FA-2 constitutes minor intervals in the AR/D member (Fig. 13). It is formed primarily of LFT-4 and LFT-5, with interbeds of LFT-3, all of which possess invariably distinctive poor sorting with bimodal or polymodal grain size and matrix-supporting to muddy-grain-supporting fabric. They contain a unique faunal assemblage of large unrolled fossils mixed with very small benthic forams and ostracods of near-shore affinity, representing strong criteria for a rapid deposition after intermittent and short-lived storms.

FA-3: Outer Ramp-Offshore Association. This association builds approximately most of the succession of the AR/D member except the pay zone (Fig. 13). It encompasses the lutitic-grained and mud-supported LFT-6 and LFT-7 in alternate units, forming together cleaning-up cycles or parasequences

that commonly stack vertically in aggradational to progradational patterns. They have commonly nodular and lenticular bedforms showing mechanical- and chemical-compaction deformations, and contain echinoids, planktonic forams, and delicate bivalves denoting a deposition in quiet, open marine water and below the SWB (Fig. 13).

Depositional Effect on AR/D Reservoir

The depositional analyses clarified that the accretion and vertical distribution of the AR/D reservoir-forming shoal/mid-ramp facies were primarily related to a prevailing paleogeography in the study area during the Turonian age. Throughout most of the time of the AR/D deposition, the Abu Sennan area was a part of an outer-ramp offshore belt of a carbonate ramp system. The majority of AR/D limestones were accreted in this belt under approximately steady rates of accommodation creation and climatic change. Consequently, the deposition proceeded without a drastic lateral shift of the other adjacent ramp sub-environments, except in a single relatively short-lived event during which a basin-ward shift of the ramp belts occurred; the Abu Sennan area first became a part of stormy mid-ramp belt that is gradually overlapped by shallow inner-ramp shoals. This event explains the limited occurrence of the reservoir facies all over the AR/D succession. Moreover, the short-lived sedimentation in the shoal belt developed well-sorted and grain-supported benthic foraminiferal peloidal packstone facies measuring a relatively enhanced porosity (15 to 27%) and a minor increase in permeability (up to 2.3 mD), with a direct relationship between poroperm character and abundance of micritic-walled forams, behamite peloids, and grainy fabric.

AR/D Diagenetic Alterations

Table 1 summarizes, in a paragenetic sequence, the various diagenetic processes and related modifications affected on AR/D carbonates since its deposition and throughout different diagenetic environments and burial stages. The net results of those processes were a severe destruction of the primary interparticles macro- and meso-pores, a near-complete occluding of the intraparticles primary and secondary voids/vugs, mechanical and chemical compaction-related deformation structures, and the formation of permeability barriers of pressure solution seams. Microscopic irregular and open fractures with few isolated intraparticles and small solution vugs and intercrystalline voids represent only the positive diagenetic products, although they are insignificant in enhancing the poroperm property of AR/D reservoir.

Table 1—Different diagenetic alterations affected on the AR/D carbonate reservoir.

Diagenetic parasequence		Eugenetic		Mesogenetic		Representative photoes
Diagenetic Processes	Diagenetic Products	Marine	Meteoric	Shallow burial	Deep burial	
1- Micritization	1.1 Bahamite peloids					
	1.2 Micrite envelope					
2- Dissolution of aragonite grains	2.1 mouldic cavities					
3- Recrystallization of micrite	3.1 Micro & pseudospars filling inter-and intraparticles pore spaces					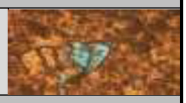
4- Early calcite cementation	4.1 Equant to drusy calcite filling mouldic cavities					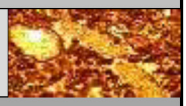
	4.2 Syntaxial overgrowth					
	4.3 Blocky calcite cement					
5- Mechanical compaction	5.1 Close packing of grain, dewatering, reduction in thickness, porosity and permeability, plane-and sutured boundaries and grain-bending or fracturing	UC	LC	C	C	
6- Chemical compaction	6.1 Pressure solution seams					
7- Late corrosion	7.1 mouldic cavities and vugs					
8- Late stage cementation and replacement	8.1 Medium to coarse crystalline dolomite, blocky calcite, Baroque dolomite, and mega-quartz & pyrite					
9- Oil migration						
10- Fracturing						

C = common, LC= less common, UC= uncommon

AR/D Reservoir Poroperm System

AR/D Poroperm Plot and Reservoir Type. The crossplot between porosity (ϕ %) and horizontal permeability (Kh) measured from 56 representative core plugs covering the entire cored section of the AR/D reservoir interval shows a wide spectrum of porosity, ranging from 1.5 to 26.4%, and Kh ranging from 0.01 to 2.3 mD with a weak direct relationship between them (Fig. 1). Approximately half (27 samples) of the measured core plugs read horizontal permeability values exceeding 0.1 mD, with the

majority measure porosity values of more than 15%. Most of these plugs are cut from the beds of shoal facies (LFT-1 and LFT-2) and mid-ramp facies (LFT-4 and LFT-5), and exist above the measured depth of approximately 1751 m. The remainder of the samples (29 samples) indicate porosity values of less than 15% and Kh of less than 0.1 mD; most of these samples were cut from the cored intervals composed of offshore outer-ramp facies (LFT-6 and LFT-7). Accordingly, the AR/D LFT-1, LFT-2, LFT-4, and LFT-5 can be ranked as low to moderately permeable reservoir facies, whereas LFT-6 and LFT-7 belong to a tight unconventional reservoir type (Fig. 1).

AR/D Reservoir Pore System. Petrographic inspection and resistivity image interpretation documented that, except for a very limited and insignificant occurrence of visible small and isolated intraparticles solution vugs, intercrystalline solution voids, and microscopic irregular open cracks, most of the primary inter- and intra-particles pores, voids, and secondary moldic cavities are completely occluded either by micrite, micro- and pseudo-spars, or successive generations of nonferoan- and feroan calcite, sucrose, and baroque dolomites, and occasionally spherulitic quartz with framboidal pyrite (Fig. 14). This means that the major part of the AR/D reservoir porosity that was either measured from core plugs or visually estimated from porosity logs is of an intercrystalline microporosity type. This assessment was confirmed by pore throat diameters that range from 0.005 to 1, as measured by mercury injection tests on four representative samples (Fig. 15). Consequently, the AR/D pay zone belongs to microporous tight to low- permeable carbonate reservoirs. Clark et al. (2008) recognized three types of microporosity; type-I, type- II, and type-III. This classification is useful in distinguishing microporosity that is effectively tight (types II and III) from that which can store and flow hydrocarbons (type I). Fullmer et al. (2014) attributed the differences between the three types of micropores to morphology and texture of micrite rhombs and related inter-crystal pores (Fig. 16). In some carbonate reservoirs, these micropore types can make up the bulk of, if not all of, the pore volume (Barnett et al. 2010).

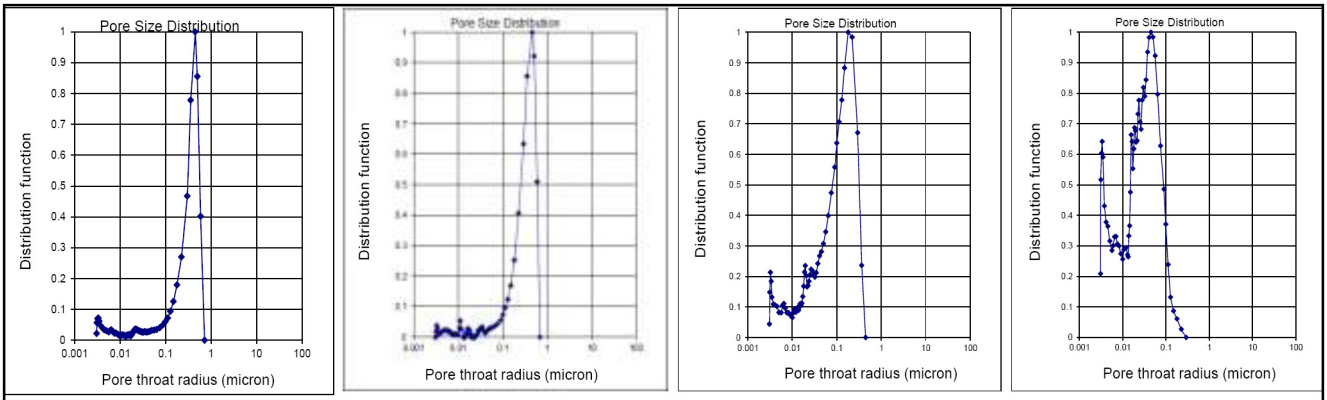

Sample Identification	2	
Sample Depth	1743.25	m.
Plug Permeability (Air)	2.5	mD
Plug Porosity (He)	0.263	fraction
Injection Sample Porosity	0.267	fraction
Injection Sample Pore Vol	0.334	cc
Injection Sample Bulk Vol	1.251	cc
Injection Sample Weight	2.887	g

Sample Identification	9	
Sample Depth	1745.00	m.
Plug Permeability (Air)	0.55	mD
Plug Porosity (He)	0.15753761	fraction
Injection Sample Porosity	0.183	fraction
Injection Sample Pore Vol	0.328	cc
Injection Sample Bulk Vol	1.793	cc
Injection Sample Weight	2.737	g

Sample Identification	18	
Sample Depth	1747.25	m.
Plug Permeability (Air)	0.1	mD
Plug Porosity (He)	0.12143735	fraction
Injection Sample Porosity	0.110	fraction
Injection Sample Pore Vol	0.147	cc
Injection Sample Bulk Vol	1.342	cc
Injection Sample Weight	3.291	g

Sample Identification	35	
Sample Depth	1751.50	m.
Plug Permeability (Air)	0.0	mD
Plug Porosity (He)	0.026	fraction
Injection Sample Porosity	0.051	fraction
Injection Sample Pore Vol	0.058	cc
Injection Sample Bulk Vol	1.129	cc
Injection Sample Weight	3.194	g

Figure 14—Mercury injection tests on four representative samples; the three samples from left represent ramp-shoal/mid-ramp facies types 1, 2, and 4, respectively, with pore throat radii ranging between 0.1 and 1μ. The fourth sample represents outer-ramp facies type 7, with pore throat radii ranging between 0.1 and 0.001μ. Notice the effect of the pore throat radius on measured permeability.

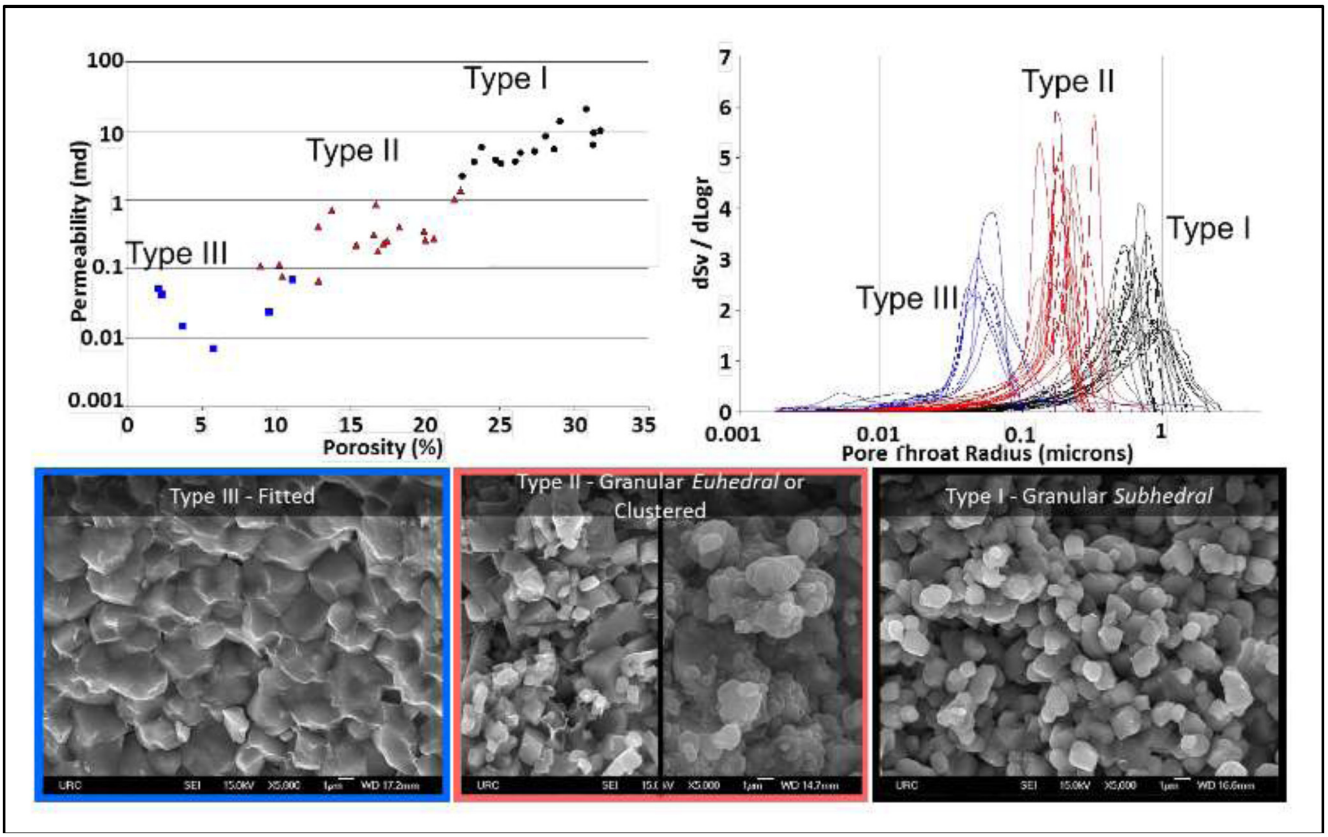

Figure 15—Crystal texture, pore throat size, and porosity-permeability relationships for Type-I, Type-II and Type-III micropores (Fullmer et al. 2014).

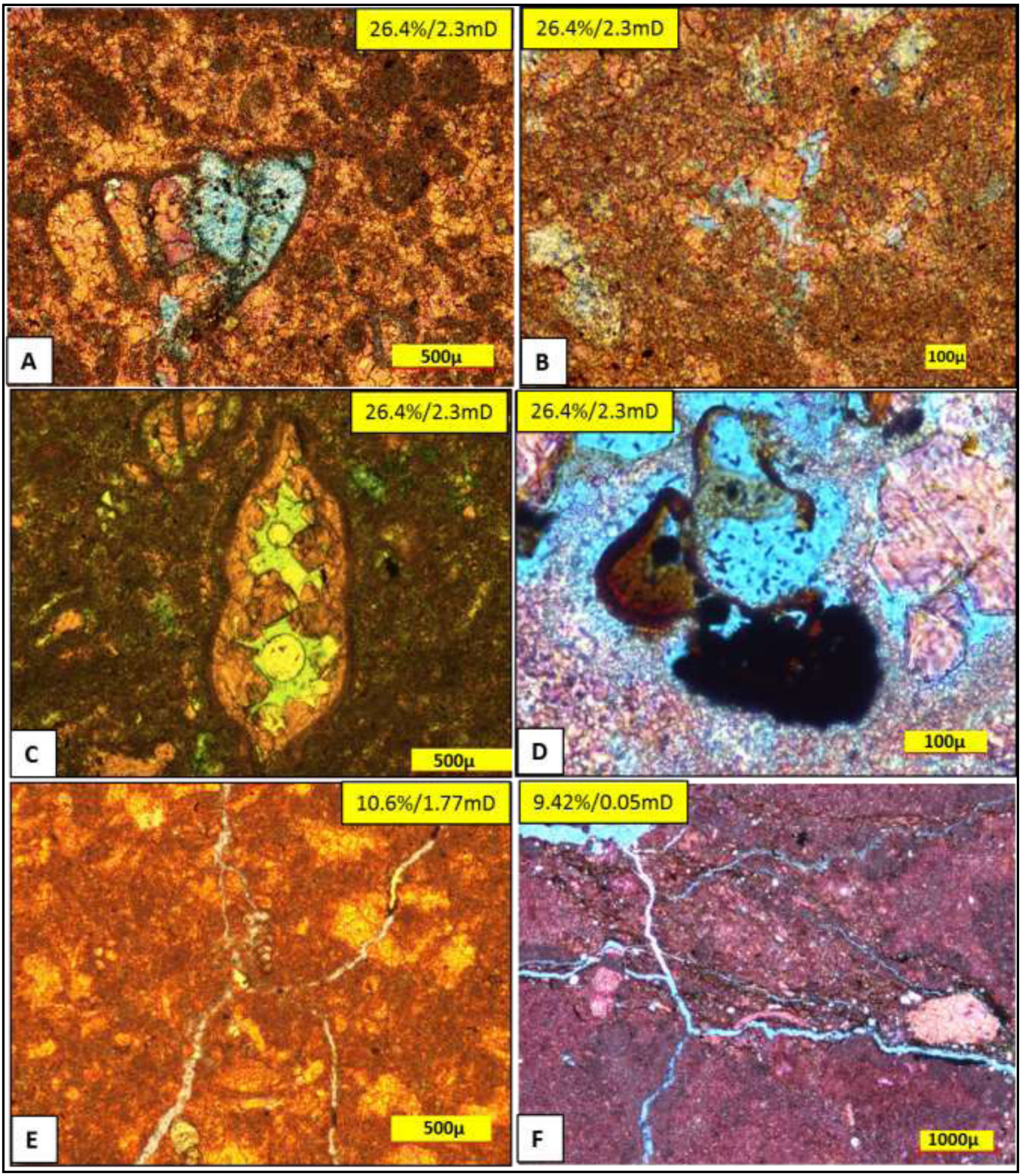

Figure 16—A) Isolated and small solution vugs preserved in a foram chambers, PPL. B) Isolated and small intercrystalline voids, PPL C) Isolated and small remnants of intercrystalline voids within calcitic bio-mold, PPL. D) Close-up view of a remnant of intercrystalline voids partially filled by orthospar, residual hydrocarbon, and framboidal pyrite. E) and F) Irregular intersecting microscopic cracks locally dissect AR/D reservoir facies without a significant effect on its poroperm property, PPL. (9.42%=measured helium porosity from core plugs, 0.05 mD=horizontal permeability, PPL=plane polarized light).

In the AR/D reservoir, the noticeable decline in the total porosity and horizontal permeability, as progressing from an inner-ramp foraminiferal peloidal packstone to an outer-ramp fine-grained bioclastic mudstone-wackestone, can be attributed to microporosity types (I-III), which are closely related to depositional fabric, texture, allochem composition, and diagenetic alterations. The highest porosity (15 to 26%) and horizontal permeability (0.5 to 2.3 mD) measured from the inner-ramp LFT-1 and LFT-2 are related to a predominance of type-I micropores, which seems to be concentrated in the micritic walled benthic forams, algae, and behamite peloids. Conversely, the crystalline orthospar and pseudospar occurring in patches between and within allochems, as well as the micrite matrix, may enclose micropores of type II and or III. This selective occurrence of micropores types is interpreted from the apparent direct relationship between poroperm values and abundance of micritic walled/micritized allochems and grain-supporting fabric. It is also evident from mercury porosimetry, which shows a prevalence of micropores with the widest pore throat radii (0.5 to 1) in foraminiferal peloidal packstone facies, whereas in the outer ramp wackestone-mudstone facies lacking micritic- walled benthic forams/peloids, the micropores have narrower throat radii ranging between 0.1 and 0.005 (Fig. 14). The SEM inspection of representative samples of the different facies belts also documented the predominance of granular subhedral micrite rhombs with type-I micropores in LFT-1, whereas the outer-ramp LFT-7 is dominated with fitted to euhedral cluster rhombs with types II-III micropores (Fig. 17). The relatively enhanced poroperm property of the inner-ramp shoal facies may be related to a late stage diagenetic corrosion of the micrite crystals building the walls of benthic forams, algae, and behamite peloids and a formation of type-1 micropores. The original inherited tiny porous micro-skeletal structures of those allochems assisted burial corrosion. Similar enhanced microporous carbonate reservoir by burial corrosion was reported in Panna and Mukta field, India by Barnett et al. (2010).

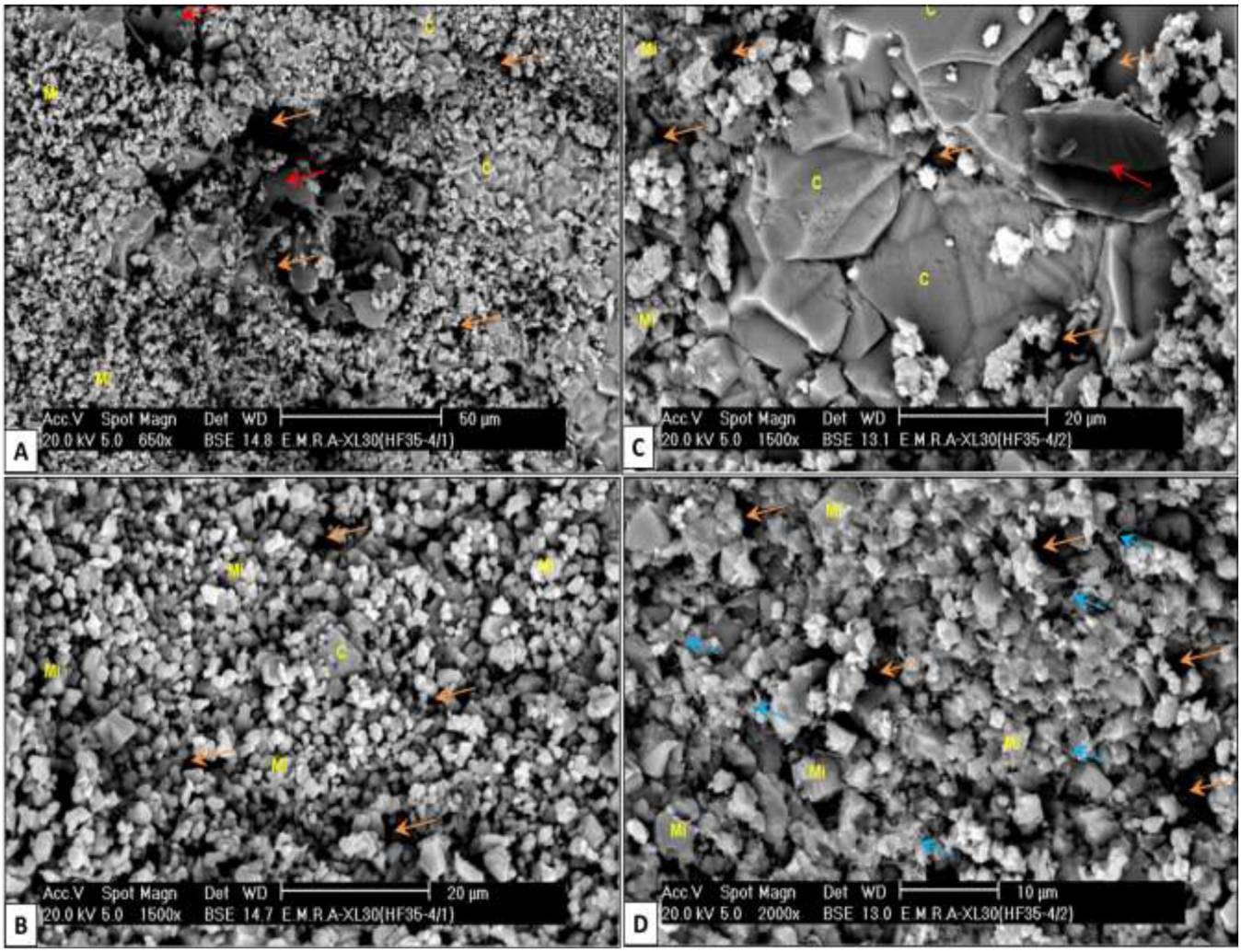

Figure 17—A) and B) SEM photos of LFT-1 consisting dominantly of subhedral micrite and microspar rhombs that have distinct granular fabric with abundant inter-rhombs micropores of type-I. C) and D) SEM photos of LFT-7 composed essentially of euhedral micrite/microspar, as well as large calcite rhombs having interlocked and fitted clusters texture with intercrystalline micropores of type II and III (Mi=microspar, C=authigenic calcite, orange arrows=micropores, red arrow=residual hydrocarbon, blue arrows=authigenic hair-like clays).

AR/D Image-Derived Poroperm Zonation using Image-Perm Software Algorithm. Image-perm is an unconventional technique that applies a borehole resistivity image to derive a continuous output of a high resolution porosity and porosity distribution map. Its concept relies on the ability to transform the high resolution conductivity data sampled by a resistivity imager from the borehole to a porosity map and porosity histograms, based simply on the relationship between porosity and resistivity in the Archie equation in the flushed zone (Newberry et al. 1996) (Fig. 18). In this technique, the porosity computation from the borehole images is constrained by an external porosity ϕ_{ext} (primarily neutron- density crossplot porosity (PXND)). The computed image porosity data from all resistivity tool pads over a sliding window of 1.2 in. is then used to compute a porosity histogram (Fig. 19A) that displays the distribution nature of porosity range across the borehole wall (homogeneous or heterogeneous). Across a homogeneous carbonate interval, the porosity range of the histogram is narrow and unimodal; the porosity range for a heterogamous interval is generally broad, polymodal, or bimodal. In addition to computing image porosity, the image-perm software algorithm can determine permeability based on high resolution image-derived porosity and the concept of petrophysical rock fabric (PRF) classes of Lucia (1999) by applying the Lucia-Jennings equation (Fig. 19B). However, the PRF classes of Lucia (1999) were

introduced for non-vuggy carbonate reservoirs with interparticles porosity. Because the AR/D carbonate reservoir belongs to a microporous reservoir family, intrinsic PRF numbers are determined and used only for this reservoir in the study field (Fig. 19C); they cannot be used for other reservoirs or for the same reservoir in other, far distant fields.

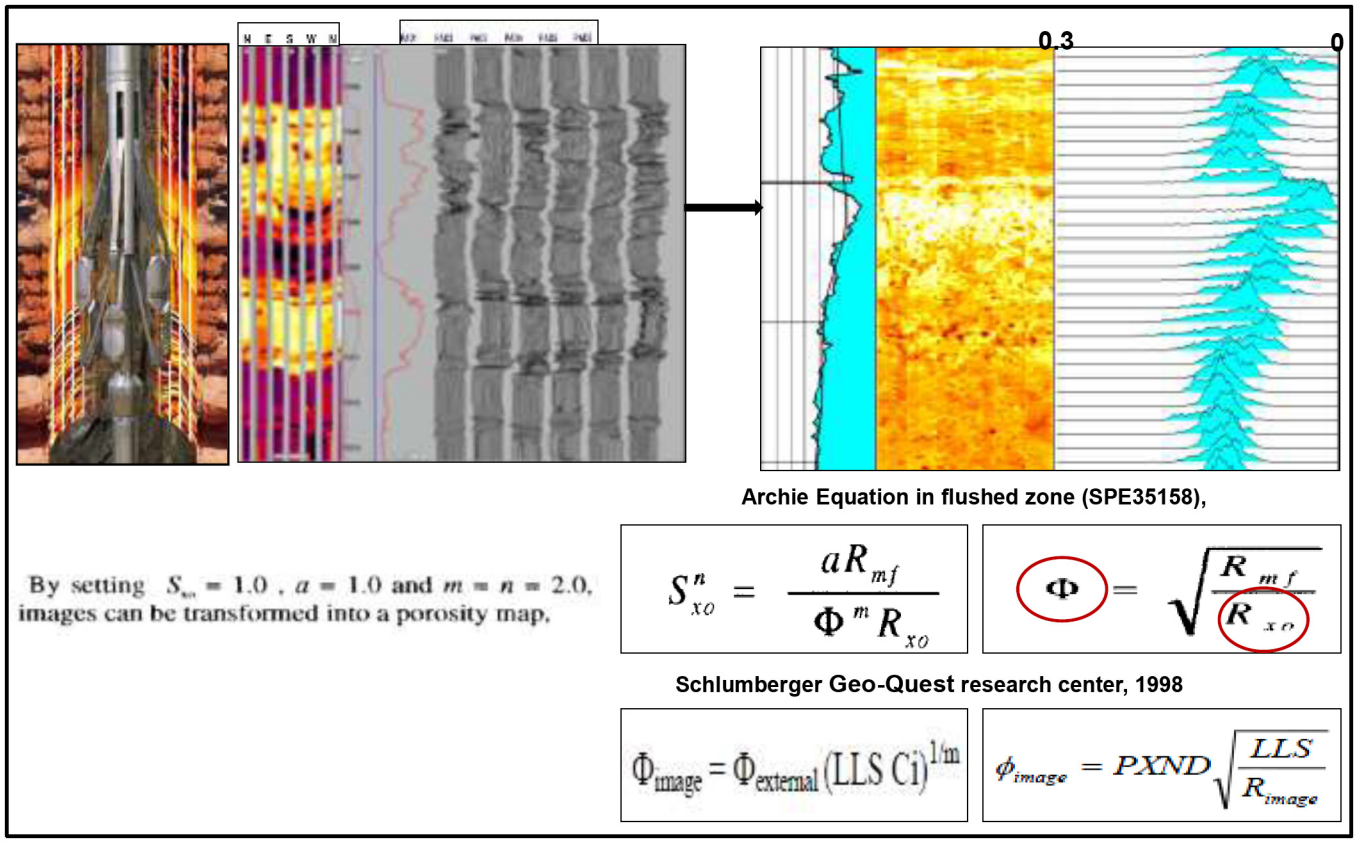

Figure 18—Concept of image-derived porosity using image-perm technique.

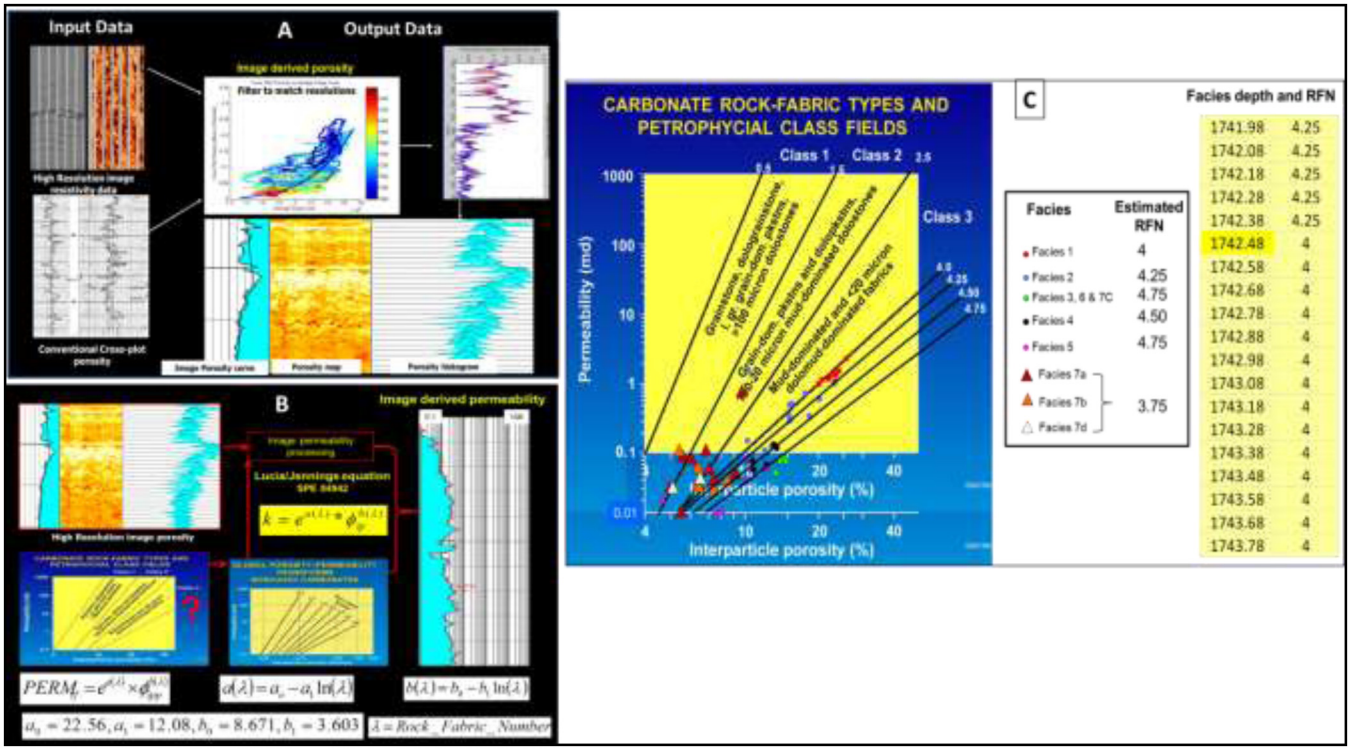

Figure 19—A) Input and output data involved in computing image-derived porosity. B) Input and output data involved in computing image-derived permeability. C) Estimated petrophysical rock fabric numbers (PRFN) for AR/D reservoir facies.

The generated image-perm plot of the AR/D reservoir interval (1740 to 1752 m) shows four distinct image poroperm zones defined based on derived high resolution image porosity, computed permeability, porosity map, and porosity distribution histograms (Fig. 20). Zone 1 is the best reservoir interval with the highest poroperm values and paramount homogeneity of narrow porosity range distribution, followed by zone 2 and zone 3. Zone 4 exhibits the poorest porosity and permeability and the highest heterogeneity. The relatively highest poroperm and unimodal porosity distribution that distinguishes zone 1 are related to a population of micritic walled fossils and behamite peloids with good sorting, and grain-supporting fabric characterizing LFT-1 and LFT-2 building this zone. Conversely, the high heterogeneity with poor poroperm values of zone 4 are linked to a noticeable decrease in large micritic walled fossils and peloids, bimodal grain size, and pervasive selective recrystallization and cementation reflected by abundant resistive laminae and patches in the porosity map and broad polymodal pattern in the porosity histogram (Fig. 20).

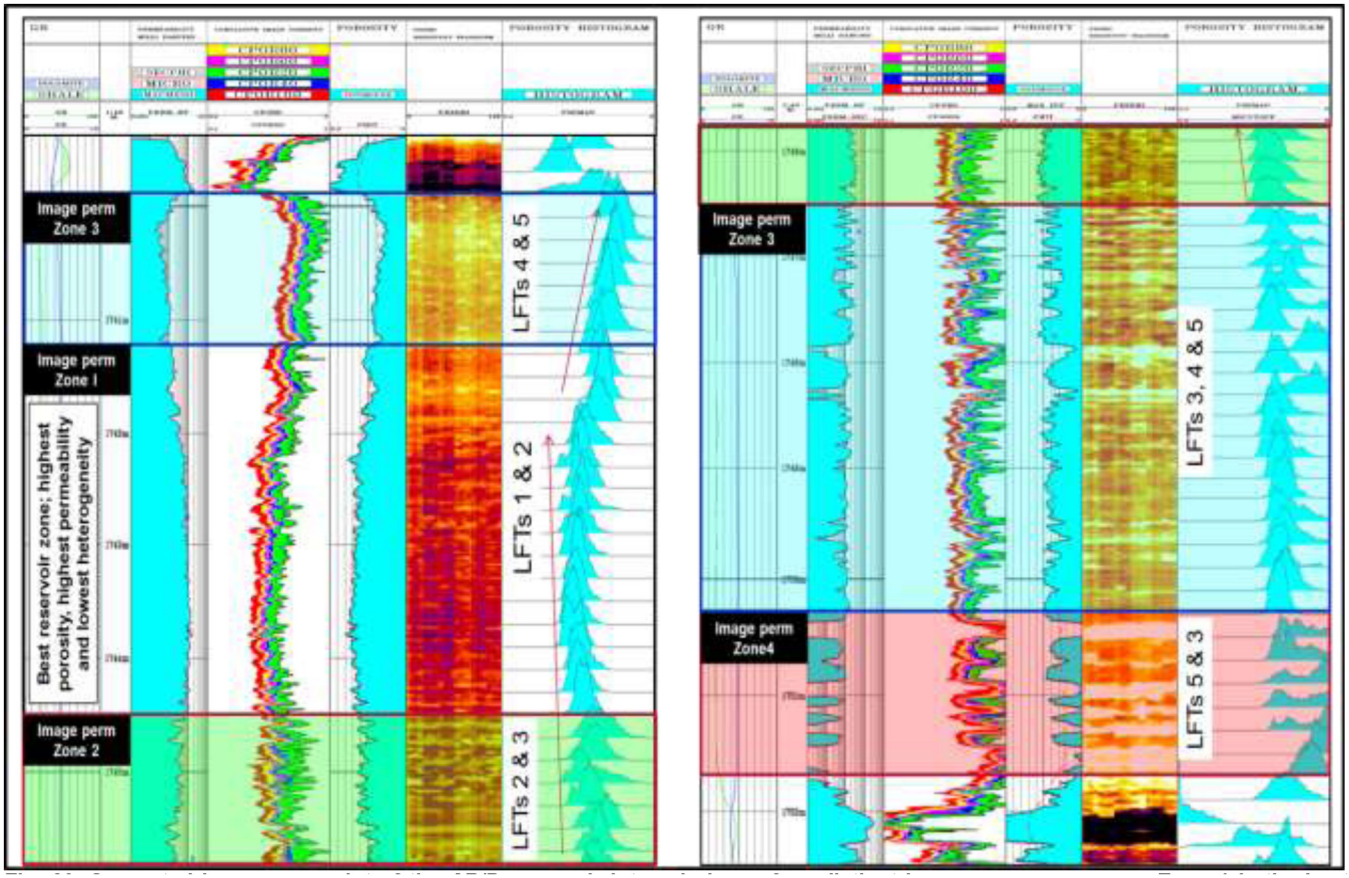

Figure 20—Generated image-perm plot of the AR/D reservoir interval shows four distinct image-poroperm zones. Zone 1 is the best zone with highest poroperm values and paramount homogeneity, followed by zone 2 and zone 3; zone 4 is the least promising zone (The permeability track scale is from 0.001 to 1mD).

Effect of AR/D Reservoir Poroperm System on Oil Recovery. As revealed from poroperm analysis, the major part of the AR/D reservoir pore system consists of intercrystalline microporosity types with a homogenous distribution, especially in zones 1 through 3 (Fig. 20). Fullmer et al. (2014) recorded that the remaining oil saturation in microporous limestone, as measured from centrifuge capillary pressure and steady state core flood experiments, is negatively correlated with the percent fraction of microporosity (Fig. 21); reservoir rocks dominated with homogeneous microporosity have more favorable oil recovery than rocks with mixed heterogeneous pore systems. Accordingly, the homogeneous and volumetrically

significant microporosity nature of AR/D reservoir may provide a favorable recovery if a suitable fracturing design is applied, and this study recommends fracturing zones 1 through 3 of the reservoir interval to enhance its oil recovery from the study well.

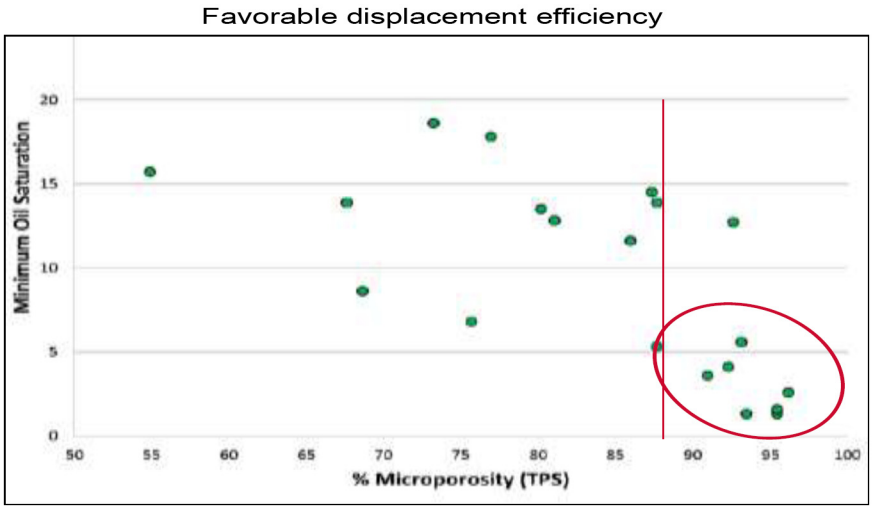

Figure 21—Crossplot of minimum oil saturation vs. microporosity percentage displays a favorable displacement efficiency of homogeneous microporous limestone reservoir (Fullmer et al. 2014).

Conclusions

In the southwestern block of Abu Sennan field, north Western Desert, Egypt, the Turonian Abu Roash D carbonate member is formed almost entirely of offshore outer-ramp wackestone-mudstone facies, except for a reduced reservoir-forming interval (approximately 10 m thick) in its lower part that consists of inner-ramp shoal to mid-ramp facies. This reservoir interval hosts and produces oil, but with extremely poor recovery. The petrographic inspection and resistivity image interpretation showed a paucity of visible inter- and intra-particles pores, significant natural open fractures, or separate/touching solution vugs. Consequently, the major part of the reservoir pore system is of intercrystalline microporosity types (I-III), with pore throat radii ranging between 1 and 0.005. The study documented the prevalence of granular type-I micropores in the shoal facies, whereas the outer ramp facies is dominated with types II and III micropores.

The AR/D reservoir is ranked as a tight- to low-permeable microporous limestone reservoir; its poroperm property is controlled by depositional fabric, allochem types, intensity of cementation/recrystallization, and the types of micro-pores. Secondary macro-/meso-pores and micro-fractures have very little distribution and play an insignificant role in enhancing its poroperm character.

The generated image-perm plot of the AR/D reservoir interval shows four distinct image-poroperm zones. Zone 1 is the best reservoir zone with highest poroperm values and paramount homogeneity of porosity range distribution, followed by zone 2 and zone 3; zone 4 contains the poorest porosity and permeability, and highest heterogeneity. The homogeneous and volumetrically significant microporosity of the AR/D reservoir may provide a favorable recovery if a suitable fracturing design is applied.

References

Ahr, W.M. 1973. The Carbonate Ramp-An Alternative to the Shelf Model. *Trans., Gulf Coast Assoc. Geol. Soc.,* **23**: 221–225.

Aigner, T. 1985. Storm Depositional Systems. In: *Lecture Notes in Earth Sciences.* **3**. Springer, Berlin, 174 p.

Arnaud-Vanneau, A., 1980. Micropaléontologie, Paléoécologie et Sédimentologie d'une Plate-Forme Carbonatée de la Marge Passive de la Téthys: L'Urgonien du Vercors Septentrional et de la Chartreuse (Alpes occidentales). *Géologie Alpine, mém.* **11,** 874 p.

Barnett, A.J., Wright, V.P., and Khanna, M. 2010. Porosity Evolution in the Bassein Limestone of Panna and Mukta Fields, Offshore Western India: Burial Corrosion and Microporosity Development. *Adapted from poster presentation at AAPG Annual Convention and Exhibition,* New Orleans, Louisiana, USA, 11-14 April.

Bayoumi, A.I., and Lotfy, H.I. 1989. Modes of Structural Evolution of Abu Gharadig Basin, Western Desert of Egypt, as deduced from seismic data. *Review Journal of African Earth Sciences,* **9**: 273–287.

Burchette, T.P. and Wright, V.P. 1992. Carbonate Ramp Depositional Systems. *Sediment. Geol.* **79**: 3–57.

Clark, D.N. 1980. The Diagenesis of Zechstein Carbonate Sediments. In H. Fuchtbauer and T. Peryt (Eds.) The Zechstein Basin with Emphasis on Carbonate Sequences. *Contributions in Sedimentology* **9**: 167–203.

Fullmer, S.M., Guidry, C.A., Gournay, J., Bowlin, E. et al, 2014. Microporosity: Characterization, Distribution and Influence on Oil Recovery. Presented at the International Petroleum Technology Conference, Doha, Qatar, 19-22 January. Paper IPTC 17629. http://dx.doi.org/10.2523/IPTC-17629-MS.

Kovács, J.S. 2005. Depth Gradient Proxies: Palaeoecology Versus sedimentology. Case Study from the Turea Group Deposits of the Paleogene Transylvanian Basin. *Acta Palaeontologica Romaniae,* **5**: 259–276.

Lucia, F. J. 1999. *Carbonate Reservoir Characterization*: Berlin, Springer-Verlag, 222 p.

Norton, P. 1967. Rock Stratigraphic Nomenclature of the Western Desert, Egypt (Internal Report). General Petroleum Corporation of Egypt.

Newberry, B.M., Grace, L.M., and Stief, D.O. 1996. Analysis of Carbonate Dual Porosity Systems from Borehole Electrical Images. Presented at the Permian Basin Oil and Gas Recovery Conference, Midland, Texas, USA. 27-29 March. Paper SPE 35158. http://dx.doi.org/10.2118/35158-MS.

Palermo, D., Aigner, T., Nardon, S., and Blendinger, W. 2010. Three-Dimensional Facies Modeling of Carbonate Sand Bodies: Outcrop Analog Study in an Epicontinental Basin (Triassic, Southwest Germany). *AAPG Bulletin,* **94** (4): 475–512.

Passey, Q.R., Bohacs, K.M., Esch, W.L., Klimentidis, R. et al, 2010. From Oil-Prone Source Rock to Gas-Producing Shale Reservoir - Geologic and Petrophysical Characterization of Unconventional Shale-Gas Reservoirs. Presented at the CPS/SPE International Oil and Gas Conference and Exhibition in China, Beijing, China, 8-10 June.

Read, J.F. 1985. Carbonate Platform Facies Models. *Bull. Am. Assoc. Pet. Geol.,* **69**: 1–21.

Sestini, G. 1995. Egypt. In Kulke, H. (Ed.), *Regional Petroleum Geology of the World, Part II: Africa, America, Australia and Antarctica.*

(V. Beiträge zur regionalen Geologie der Erde, Band 22, p. 66–87, *Gebrüder Bornträger Verlagsbuchhandlung,* Stuttgart.

Wilson, J. L. 1975. *Carbonate Facies in Geologic History.* Springer-Verlag, New York, 471 p.

Wright, V.P. and Burchette T.P. 1998. Carbonate Ramps. *Geol. Soc. Lond. Spec. Publ.* **149**: 1–462.

Zobaa, M.K., Oboh-Ikuenobe, F.E. and Ibrahim, M.I. 2011. The Cenomanian/Turonian Oceanic Anoxic Event in the Razzak Field, North Western Desert, Egypt: Source Rock Potential and Paleoenvironmental Association. *Marine and Petroleum Geology* **28** (8): 1475–1482.